The upper Oligocene San Rafael intrusive complex (Eastern Cordillera, southeast Peru), host of the largest-known high-grade tin deposit

Matthieu Harlaux, Kalin Kouzmanov, Stefano Gialli, Alan Clark, Oscar Laurent, Guillaume Corthay, Esteban Prado Flores, Andrea Dini, Alain Chauvet, Alexey Ulianov, et al.

LITHOS 400-401 (2021) 106409

Contents lists available at ScienceDirect

LITHOS

journal homepage: www.elsevier.com/locate/lithos

Research article

The upper Oligocene San Rafael intrusive complex (Eastern Cordillera, southeast Peru), host of the largest-known high-grade tin deposit

Matthieu Harlaux [a,b,*], Kalin Kouzmanov [a], Stefano Gialli [a], Alan H. Clark [c], Oscar Laurent [d,1], Guillaume Corthay [a], Esteban Prado Flores [a], Andrea Dini [e], Alain Chauvet [f], Alexey Ulianov [g], Massimo Chiaradia [a], Andrew Menzies [h], Gustavo Villón Durand [i], Miroslav Kalinaj [i], Lluís Fontboté [a]

[a] Department of Earth Sciences, University of Geneva, 1205 Geneva, Switzerland
[b] Nevada Bureau of Mines and Geology, University of Nevada, Reno, NV 89557-0178, USA
[c] Department of Geological Sciences and Geological Engineering, Queen's University, Kingston, ON K7L 3N6, Canada
[d] Institute of Geochemistry and Petrology, ETH Zürich, 8092 Zürich, Switzerland
[e] Istituto di Geoscienze e Georisorse, CNR, 56124 Pisa, Italy
[f] Géosciences Montpellier, CNRS-UMR 5243, Université de Montpellier, 34095 Montpellier, France
[g] Institute of Earth Sciences, University of Lausanne, 1015 Lausanne, Switzerland
[h] Bruker Nano GmbH, Am Studio 2D, 12489 Berlin, Germany
[i] Minsur S.A., Jr. Lorenzo Bernini 149, San Borja, Lima 27, Peru

ARTICLE INFO

Keywords:
San Rafael deposit
Central Andes
Peraluminous granites
Magma mixing
Tin mineralization

ABSTRACT

The upper Oligocene San Rafael intrusive complex (SRIC), located at the southwest margin of the Eastern Cordillera of southeast Peru, is an exceptional case study to investigate the petrogenesis of a large composite granitic pluton associated with the largest known high-grade Sn deposit (>1 Mt. Sn). The granitic rocks are quasi-continuously exposed over more than 1.4 km vertically, from the cupola at surface to deeper levels in the underground mine workings, thus providing access to the upper part of a large pluton. We describe new field relationships and petrographic observations of the main granite varieties of the SRIC, and we report quantitative mineral analyses, whole rock geochemistry (major and trace elements, radiogenic Sr, Nd, and Pb isotopes), and in situ U—Pb dating and trace element analysis of zircons. The SRIC is dominantly composed of a biotite-cordierite -bearing K-feldspar megacrystic granite, which contains comagmatic enclaves and dismembered dikes of fine-grained and medium-grained granites, and subordinate lamprophyres. While the granitic rocks are widely affected by variable degrees of pervasive hydrothermal alteration, the least altered samples are characterized by moderately fractionated peraluminous S-type compositions, with similar enrichments in incompatible elements (Li, B, Ga, Rb, Sn, Cs, Th, and U), relatively high Zr/Hf and Nb/Ta ratios, and strongly crustal Sr, Nd, and Pb isotopic signatures. In situ U—Pb dating and trace element analysis of zircons indicate that the granitic magmas crystallized contemporaneously within age uncertainty at 24.02 ± 0.25 Ma (megacrystic granite), 24.17 ± 0.28 Ma (fine-grained granite), and 24.26 ± 0.26 Ma (medium-grained granite) at Ti-in-zircon temperatures from 638° to 840 °C (avg = 759 ± 49 °C). The lamprophyres have high contents of lithophile elements (Li, Rb, Cs, Sn, W) while showing more primitive Sr—Nd isotopic compositions, indicating a metasomatized subcontinental lithospheric mantle source contaminated by crustal assimilation and/or mixing with granitic magmas. Tin contents of the main San Rafael granites are moderate (3–40 ppm; avg. = 13 ppm Sn) and fall in the same range of values as reported for "tin granites" from the Central Andean tin belt. Based on our petrological and geochemical data, we conclude that the SRIC results from multiple injection and mingling/mixing of several types of coexisting felsic and mafic magmas in a shallow-crustal reservoir. The granitic magmas were largely derived from partial melting of metasedimentary protoliths and hybridization with mantle-derived mafic melts, in a regional geodynamic setting dominated by anomalous asthenospheric heat flow beneath the southern

* Corresponding author at: Nevada Bureau of Mines and Geology, University of Nevada, Reno, NV 89557-0178, USA.
E-mail address: mharlaux@unr.edu (M. Harlaux).
[1] Present address: Géosciences Environnement Toulouse, CNRS-UMR 5563, Observatoire Midi-Pyrénées, Université Toulouse III Paul Sabatier, 31400 Toulouse, France.

https://doi.org/10.1016/j.lithos.2021.106409
Received 24 November 2020; Received in revised form 28 July 2021; Accepted 29 July 2021
Available online 6 August 2021

Peruvian Altiplano during the Oligocene to Miocene. Based on the moderately fractionated peraluminous character of the SRIC, we conclude that the granitic pluton was a passive host for Sn mineralization and only provided the structural focusing for metal-rich magmatic fluids derived from a deeper part of the granitic magma reservoir. We propose a model in which the injection of high-temperature mafic melts into a more reduced, fractionated granitic magma reservoir triggered late-magmatic oxidation, crystal mush reactivation, and exsolution (second boiling) of metal-rich magmatic fluids. The latter ascended toward the upper part of the crystallized granitic pluton and were focused along subvertical dilational structures, where they cooled down and mixed with downwelling meteoric waters, thus generating the world-class San Rafael Sn (—Cu) deposit.

1. Introduction

Granite-related Sn (±W) deposits are currently interpreted as resulting from highly evolved granitic magmas formed either via extended fractional crystallization from source rocks that show no initial Sn (±W) enrichment (Lehmann, 2020), or from high-temperature melting of Sn (±W)-rich thick metasedimentary sequences along continental margins (Romer and Kroner, 2016). Granitic rocks associated with Sn deposits are generally part of composite batholiths and are often interpreted to be the source of the mineralizing fluids and metals (Audétat et al., 2000; Lehmann, 2020). One major limitation for the study of these ore-forming magmatic-hydrothermal systems is that the causative intrusion is rarely exposed or identified in many Sn deposits worldwide. Often, it remains unclear whether the host intrusion is the direct source of mineralizing fluids, or the exposed granitic stock essentially provides the structural focusing for magmatic-hydrothermal fluids released from an underlying magma chamber. Additionally, granitoids spatially associated with Sn—W deposits are often affected by widespread hydrothermal alteration, which obscures the genetic relationships and limits the elaboration of comprehensive models.

This study aims to investigate the upper Oligocene San Rafael intrusive complex (SRIC) hosting the largest known high-grade Sn deposit, which produced about 26.6 Mt. ore at 3.7% Sn on average between 1969 and 2019 (Minsur, internal report). The world-class San Rafael Sn (—Cu) deposit is part of the Central Andean tin belt that extends from southeast Peru, through Bolivia, to northernmost Argentina, and contains several world-class Oligocene to Miocene Sn ± W deposits spatially related to peraluminous granitoids and subvolcanic stocks (Clark et al., 1983, 1990; Lehmann et al., 1990). These ore deposits formed in the "Central Andean Inner Arc", characterized by the production of voluminous peraluminous S-type granitic magmas, developed coevally with the steepening and/or breakoff of the oceanic slab subsequent to a period of flat subduction between the Farallon/Nazca plate and the South American continent (Clark et al., 1990; Kontak et al., 1990a; Ramos, 2018; Sandeman et al., 1995). In the Cordillera de Carabaya of southeast Peru, the Picotani Group (ca. 22–28 Ma) constitutes a diverse assemblage of granitoids and subvolcanic stocks associated with mantle-derived mafic rocks exhibiting extensive field and petrographic evidence of magma mingling and mixing (Carlier et al., 1997; Clark and Kontak, 2004; Kontak and Clark, 1997; Sandeman et al., 1995, 1997; Sandeman and Clark, 2003, 2004). Lead isotopic compositions of ore deposits from the Central Andean tin belt are similar suggesting that metals were derived from a similar crustal source (Kamenov et al., 2002; Kontak et al., 1990b; Macfarlane et al., 1990).

In the present paper, we describe new field relationships and petrographic observations of the SRIC, which is exceptionally well exposed at surface and in the underground workings over a total vertical and lateral extent of ca. 1.4 and 5 km, respectively. Based on the different types of rocks identified, we report quantitative mineral analyses, whole rock geochemical compositions (major and trace elements, radiogenic Sr, Nd, and Pb isotopes), and in situ U—Pb dating and trace element analysis of zircons. We demonstrate that the SRIC results from multiple injection and mingling/mixing of several types of coexisting felsic and mafic magmas in a shallow-crustal reservoir. We propose that the peraluminous S-type granitic magmas were largely derived from partial melting of metasedimentary protoliths and hybridization with mantle-derived mafic melts. Based on the moderately fractionated peraluminous character and the moderate Sn contents of the San Rafael granites, we conclude that the source of the mineralizing fluids is a deeper, more fractionated, granitic magma reservoir. We further discuss the source of Sn and Cu in the San Rafael deposit and the possible role of mantle-derived mafic magmas injected into the crystal mush reservoir for triggering exsolution of metal-rich magmatic fluids.

2. Geological background

The SRIC is located in the Cordillera de Carabaya of southeast Peru, part of the Eastern Cordillera, which is a NW-trending high-elevation (up to 6000 m) mountain range located between the Altiplano to the west and the Subandean zone to the east. The San Rafael deposit is part of the northern sector of the Central Andean tin belt, which extends about 1000 km to the southeast as a 30–130 km-wide belt from southern Peru, through Bolivia, to northern Argentina (Fig. 1A). This metallogenic belt hosts hundreds of Sn-W ± Ag-Cu occurrences that are spatially associated with peraluminous granitoids and subvolcanic stocks emplaced during two major geologic periods: (i) Late Triassic - early Jurassic (ca. 220–190 Ma), restricted to the northern part of the belt; and (ii) Late Oligocene - early Miocene (ca. 26–20 Ma), affecting the entire belt (Clark et al., 1990; Gemmrich et al., 2021; Lehmann et al., 1990). The Eastern Cordillera of southern Peru is composed of a more than 10 km-thick sequence of Lower Paleozoic metasedimentary rocks assigned to the San José, Sandia, and Ananea Formations overlying unexposed Precambrian gneissic basement (Clark et al., 1990; Kontak et al., 1990a; Sandeman et al., 1995; Spiske et al., 2006). These metasedimentary rocks were intruded by Oligocene to Miocene intrusive rocks of the Crucero Supergroup, which consists of peraluminous granitoids and subvolcanic stocks associated with calc-alkaline to highly-potassic mantle-derived mafic rocks (Kontak et al., 1990a; Sandeman et al., 1997).

San Rafael currently is one of the largest and richest primary Sn deposits in the world, with total past production of >1 Mt. of Sn and >30 Kt. of Cu and additional metals (Zn, Pb, Ag). Total reserves are estimated at 8 Mt. of ore at 1.74% Sn (Minsur, internal report). The mineralization occurs as mainly NNW-SSE striking and steeply dipping toward the NE quartz-cassiterite-sulfide veins and breccia bodies, which are hosted by a peraluminous granitic complex and the surrounding Ordovician metasedimentary rocks of the Sandia Formation (Fig. 1B;Kontak and Clark, 2002; Mlynarczyk et al., 2003). The latter consist dominantly of quartz-sandstones alternating with mudstones and siltstones affected by low-grade metamorphism (Spiske et al., 2006), except in the contact metamorphic aureole of the granitic pluton where they are transformed to andalusite-bearing hornfels. The vein system extends for more than 1.4 km vertically and more than 3 km along strike, developing laterally over 5 km in a SW-NE direction as a series of subparallel lodes, mainly controlled by left-lateral motion (Kontak and Clark, 2002; Mlynarczyk et al., 2003). The SRIC consists of a peraluminous, K-feldspar megacrystic biotite-cordierite -bearing granite containing minor enclaves of granites and lamprophyres. It comprises the San Rafael granite cropping out in the southwestern part of the district and the Quenamari granite in its northeastern part, both of these granitic bodies coalescing at depth, as

indicated by deep drillings and underground workings (Fig. 1C). Porphyritic granite ring dikes occur west and southeast of the SRIC and are similar in composition to the main pluton (Kontak and Clark, 2002; Fig. 1B). Previous studies on the SRIC (Kontak and Clark, 2002; Mlynarczyk, 2005; Mlynarczyk et al., 2003) were restricted to surface exposures of the granitic rocks and to underground workings >4300 m above sea level (masl) in the San Rafael mine. This work is based on a large set of representative samples that were collected on an extended surface area of approximately 4 × 6 km at elevation >4500 masl and from underground workings of the San Rafael mine down to 3600 masl.

3. Analytical methods

3.1. Petrography and automated mineralogy (QEMSCAN)

Petrographic observations were carried out using transmitted-light microscopy combined with cold cathodoluminescence (CL) imaging to characterize mineral textures. The CL images were acquired at the University of Geneva (Switzerland) using an Cathodyne® electron cathode from NewTec Scientific, mounted on a Olympus BX41 microscope operated with an acceleration voltage of 18 kV, a gun current of 120–200 μA, and with a processing resolution of 1600 × 1200 pixels. Automated mineral analysis and textural imaging of the samples were carried out using a FEI QEMSCAN Quanta 650 F facility at the University of Geneva. The QEMSCAN system is equipped with two Bruker QUANTAX light-element energy-dispersive (EDS) detectors. Analyses were conducted in field image operating mode at high vacuum, accelerating voltage of 25 kV, and using a beam current of 10 nA on carbon-coated polished thin sections. In total, 221 individual fields were measured per sample, with a field size of 1500 × 1500 μm and a point spacing of 5 μm. The standard 1000 counts per point were acquired, yielding a limit of detection of approximately 2 wt% per element for mineral classification. Measurements were performed using the iMeasure v5.3.2 software, and the iDiscover v5.3.2 software package was used for data processing. Results consist of spatially resolved and fully quantified mineralogical maps and X-ray elemental distribution maps. Differentiation of plagioclase composition to "albite" and "plagioclase" on the QEMSCAN maps is based on the anorthite content: "albite" is used for high Na compositions (albite-oligoclase; An0–30) and "plagioclase" is used for high Ca compositions (andesine-anorthite; An30–100). The CL images and QEMSCAN maps of the studied samples are shown in Supplementary Fig. 1.

3.2. Whole rock geochemistry

Samples selected for whole rock geochemistry were crushed using a steel jaw crusher and subsequently a hydraulic press and were finally powdered to <70 μm using a mortar agate mill. Major elements were

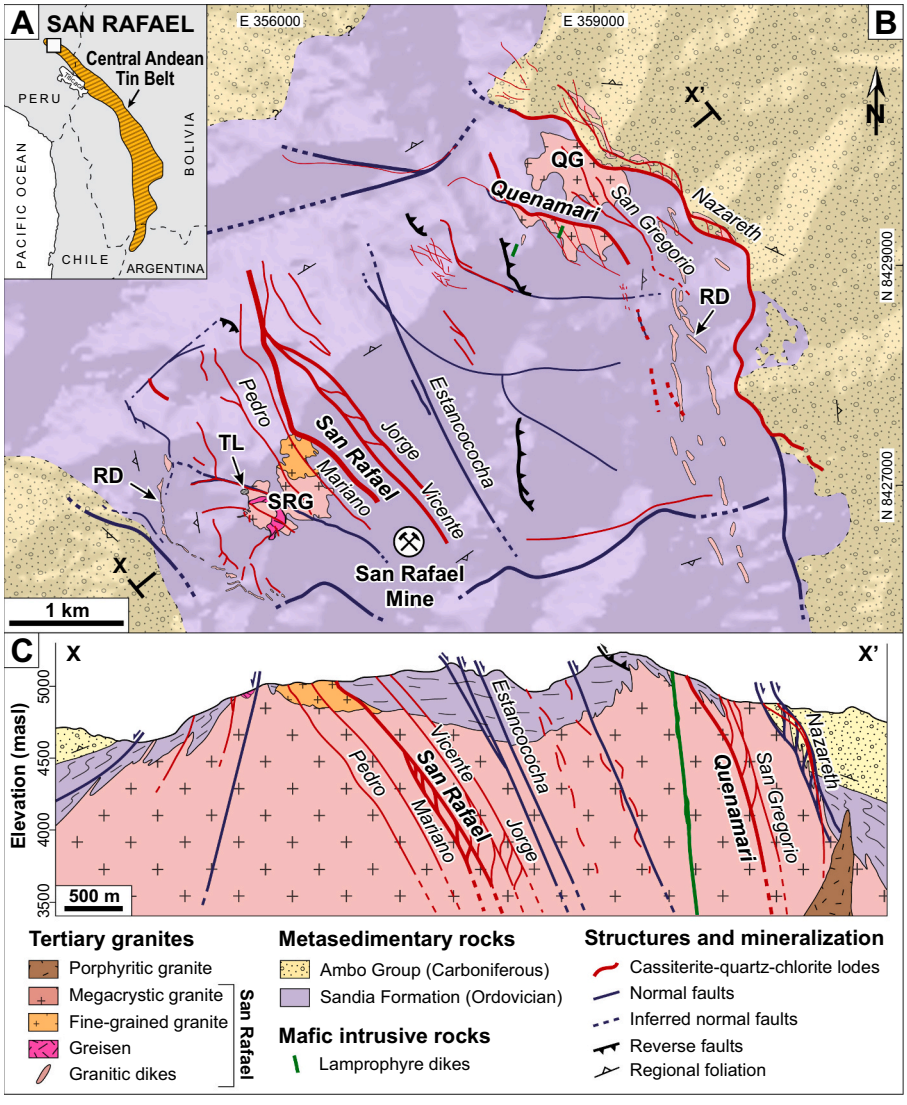

Fig. 1. Geological map and cross-section of the San Rafael intrusive complex (SRIC), Eastern Cordillera, southeast Peru. A) Location of the San Rafael Sn (—Cu) deposit in the Central Andean tin belt (modified after Mlynarczyk et al., 2003). B) Geological map and C) longitudinal cross-section of the San Rafael deposit (modified from Harlaux et al., 2020). Map line of section X-X' is shown on B). Abbreviations: SRG = San Rafael granite, QG = Quenamari granite, TL = tourmaline-bearing leucogranite, RD = ring dikes.

analyzed on pressed powder pellets by X-ray fluorescence analysis (XRF) using a Philips PW 2400 spectrometer at the University of Lausanne, Switzerland. The standards BE-N, SY-2, and BHVO were used as quality control for XRF analyses. Trace elements were measured in fused lithium tetraborate beads by laser ablation – inductively coupled plasma – mass spectrometry (LA-ICP-MS) using a NewWave UP-193 nm ArF excimer laser system attached to an Element XR (Thermo Scientific, Germany) sector-field instrument at the University of Lausanne. Laser ablation was performed with a constant 10 Hz pulse frequency, a laser spot of 150 μm, and a fluence of 5 J.cm^{-2}. The certified reference glass NIST SRM 612 was used as an external standard using conventional standard-sample bracketing to correct for sensitivity drift throughout the analytical session. Data reduction was done using the Matlab-based SILLS software (Guillong et al., 2008). The whole rock contents of B and Li were determined at Activation Laboratories (ActLabs, Canada) by Prompt Gamma Neutron Activation Analysis (PGNAA) and sodium peroxide fusion followed by ICP-MS analysis, respectively. Whole rock Sr, Nd, and Pb isotopic compositions were measured on powdered samples at the University of Geneva using a Thermo Neptune Plus Multi-Collector ICP-MS in static mode following the method described in Chiaradia et al. (2020). Analytical accuracy and long-term 1σ external reproducibility of Sr (18 ppm) and Nd (14 ppm) isotope analyses were assessed using the reference materials NIST SRM 987 ($^{87}Sr/^{86}Sr = 0.710248$) and JNdi-1 ($^{143}Nd/^{144}Nd = 0.512115$). External reproducibility (1σ) of the Pb isotope analyses assessed using the NIST SRM 981 is 0.11% for $^{206}Pb/^{204}Pb$, 0.12% for $^{207}Pb/^{204}Pb$, and 0.20% for $^{208}Pb/^{204}Pb$. Isotopic ratios were corrected for an age of 25 Ma.

3.3. U—Pb dating and trace element analysis of zircon

Samples were crushed and milled to <0.3 mm and processed using a gravity separation Wilfley table, a Frantz magnetic separator, and a density separation in diiodomethane liquid at 3.32 g.cm^{-3}. Zircon grains were handpicked under a binocular microscope, mounted in epoxy resin, and polished. Zircon grain textures were characterized by scanning electron microscopy - cathodoluminescence (SEM-CL) imaging using a JEOL JSM7001F at the University of Geneva. Analyses were conducted using an acceleration voltage of 15 kV on carbon-coated polished grain mounts. Simultaneous U—Pb isotopic and trace element analyses of zircon were carried out at the ETH Zürich (Switzerland) using a RESOlution S-155 (Australian Scientific Instruments/Applied Spectra, USA) 193 nm ArF excimer laser system attached to an Element XR (Thermo Scientific, Germany) sector-field ICP-MS. Analyses were performed on epoxy grain mounts loaded in a two-volume, fast-washout S-155 ablation cell (Laurin Technic, Australia) fluxed with carrier gas consisting of ca. 0.5 L.min^{-1} He (5.0 grade) and sample gas consisting of ca. 1 L.min^{-1} Ar (6.0 grade) from the ICP-MS and ca. 2 mL.min^{-1} N_2. Laser repetition rate of 3 Hz, spot diameter of 29 μm, and on-sample energy density of ca. 2.5 J.cm^{-2} were used. Three pre-ablation pulses were applied immediately before each analysis for surface cleaning. Signal homogenization was performed using in-house Squid tubing. The ICP-MS instrument is equipped with a high capacity (80 m^3.h^{-1}) interface pump to achieve, in combination with jet sampler and normal H-skimmer cones, a detection efficiency (based on U in NIST SRM 612 glass) of about 2% (Guillong et al., 2020). The ICP-MS was tuned using the NIST SRM 612 reference material for maximum sensitivity on the high mass range while keeping the production of oxides low ($^{248}ThO^+/^{232}Th^+$ <0.10%) and the U/Th ratio ~ 1. Intensities for the 34 following isotopes were acquired using time resolved-peak jumping and triple detector mode: ^{7}Li, ^{11}B, ^{27}Al, ^{29}Si, ^{31}P, ^{49}Ti, ^{89}Y, ^{91}Zr, ^{93}Nb, ^{118}Sn, ^{139}La, ^{140}Ce, ^{141}Pr, ^{146}Nd, ^{147}Sm, ^{153}Eu, ^{157}Gd, ^{159}Tb, ^{163}Dy, ^{165}Ho, ^{166}Er, ^{169}Tm, ^{172}Yb, ^{175}Lu, ^{178}Hf, ^{181}Ta, ^{202}Hg, ^{204}Pb, ^{206}Pb, ^{207}Pb, ^{208}Pb, ^{232}Th, ^{235}U, and ^{238}U. Dwell times were set to 10 ms, except for ^{49}Ti and ^{238}U (25 ms), ^{206}Pb and ^{207}Pb (75 ms), resulting in a total sweep time of 736 ms. Each measurement consisted of 30 s of gas blank followed by 30 s of sample ablation. Data reduction was done using the Matlab-based SILLS software (Guillong et al., 2008). The GJ-1 reference material ($^{206}Pb/^{238}U = 0.097877 \pm 0.000068$, $^{207}Pb/^{206}Pb = 0.060171 \pm 0.00005$; Horstwood et al., 2016) was used as primary standard for U—Pb dating. The reference materials 91500 (1065 Ma), Plešovice (337.13 ± 0.37 Ma), and AUSZ7–1 (38.9022 ± 0.0035 Ma) were analyzed as secondary standards to control the reproducibility and accuracy of the data and yielded weighted mean $^{206}Pb/^{238}U$ ages of 1058 ± 11 Ma (2σ, MSWD = 0.35, $n = 8/8$), 339.2 ± 3.6 Ma (2σ, MSWD = 0.69, $n = 8/8$), and 38.31 ± 0.54 Ma (2σ, MSWD = 1.5, $n = 6/8$), respectively. Uncertainties of the ages were calculated as MSWD of concordance. Data were reduced using the Iolite v2.5 software with the VisualAge data reduction scheme (Petrus and Kamber, 2012). Raw isotope ratios calculated from background-subtracted intensities were corrected for laser-induced Pb/U fractionation, instrumental mass discrimination, and drift through the analytical session by conventional standard-sample bracketing, against normalization to zircon reference material GJ-1. No common Pb correction was applied, and Pb-rich and/or discordant zircons were excluded from the U—Pb dataset. Uncertainty on ratios and ages are at 2σ absolute, including propagated uncertainty based on the within-session scatter of the primary reference material. Uncertainties on the reference values of the primary reference material, decay constants of ^{235}U and ^{238}U, and long-term excess variance of validation reference materials (1% relative) are propagated by quadratic addition to the calculated uncertainty of weighted mean ages for unknowns (Horstwood et al., 2016). For trace element quantification, the integration intervals defined for U—Pb data reduction were used to ensure that trace elements and U—Pb dates were obtained exactly from the same zircon volume. The NIST SRM 610 was used as a calibration reference material for trace element quantification via conventional standard-sample bracketing to correct for sensitivity drift throughout the analytical session. The stoichiometric Si content of zircon (15.2 wt%) was used as internal standard for relative sensitivity correction. Ti concentrations in zircon were further corrected from matrix effects by normalization to concentration in 91500 reference material (4.73 ± 0.15 ppm; Szymanowski et al., 2018).

4. Results

4.1. Field relationships and petrographic observations

Based on previous studies and the present work, we distinguish six granitic rocks in the SRIC, in addition to lamprophyre and greisen. Pervasive hydrothermal alteration is present in almost all investigated samples to variable degrees (weak, moderate, strong). The descriptions below are based on the least altered and most representative samples.

(i) *Megacrystic granite* is the volumetrically most important granitic facies building up the essential of the San Rafael and Quenamari stocks. At the pluton scale, the megacrystic granite is relatively homogeneous and no vertical or lateral zoning could be observed. The megacrystic granite is characterized by centimeter-sized phenocrysts of K-feldspar dispersed in a medium-grained (0.1–1.0 cm) groundmass of quartz, plagioclase, K-feldspar, biotite, and cordierite (Figs. 2A, 3A and 4A-B). Quartz consists of irregularly shaped and embayed phenocrysts ranging from 100 μm to a few millimeters in size. K-feldspar exhibits perthite lamellae as evidenced by microscopy and X-ray elemental mapping (Supplementary Fig. 1). Plagioclase forms subeuhedral grains of several millimeters in size and shows growth zoning characterized by Ca-rich core overgrown by Na-rich rim separated by dissolution surfaces at the core-rim interface (Fig. 4C-F). Cordierite occurs as euhedral bluish-greenish phenocrysts (up to 2 cm in diameter) and is commonly altered to pinite. Pseudospherical quartz-tourmaline nodules (average diameter of 0.5 cm), accounting for <1% of the mineral assemblage, are also present erratically in the granitic groundmass. QEMSCAN

analysis of the least altered megacrystic granite samples reports primary compositions of 19.8–35.9% quartz, 21.4–30.5% K-feldspar, 4.6–20.0% plagioclase (Ca-dominated), 11.6–14.3% albite, 4.8–8.7% biotite, and < 2% of accessory minerals including tourmaline, apatite, ilmenite, sphene, rutile, zircon, and monazite (Fig. 4; Supplementary Fig. 1). The megacrystic granite is affected by variable degrees of pervasive hydrothermal alterations, which dominantly consist of replacement of perthitic K-feldspar and plagioclase phenocrysts by hydrothermal orthoclase and muscovite (i.e., K alteration), replacement of plagioclase by hydrothermal albite (i.e., Na alteration), and chloritization of biotite (Supplementary Fig. 1). Hydrothermal muscovite, albite, chlorite, and other accessory minerals (e.g., kaolinite, epidote, calcite), altogether represent 5–8% of the least altered granitic rock samples.

(ii) *Fine-grained granite* (or microgranite) shows similar mineral assemblage as the megacrystic granite but differs by a fine-grained texture and slightly different mineral proportions (Figs. 3B and 5A). The fine-grained granite crops out in the northern part of the SRIC (Fig. 1B-C) and shows progressive gradual contacts with the megacrystic granite. It is also observed in the underground workings as comagmatic enclaves within the megacrystic granite (Fig. 2C). The granitic groundmass consists dominantly of quartz, K-feldspar, plagioclase, biotite, and cordierite with grain size ranging from 100 μm to a few millimeters. QEMSCAN analysis of the least altered fine-grained granite samples reveals primary mineral abundances of 22.0–28.4% quartz, 28.5–32.0% K-feldspar, 13.3–18.1% albite, 11.0–19.7% plagioclase (Ca-dominated), 1.6–8.6% biotite, and < 1% of accessory tourmaline, apatite, ilmenite, sphene, rutile, zircon, and monazite (Fig. 5A; Supplementary Fig. 1). Hydrothermal alteration consists of replacement of K-feldspar by hydrothermal orthoclase and muscovite, chloritization of biotite, and albitization of plagioclase phenocrysts.

(iii) *Dismembered fine-grained granitic plug* is mostly observed in the underground workings (<4500 masl) as irregular enclaves and discontinuous dikes in the megacrystic granite (Fig. 2B). In the Quenamari area, fine-grained granitic dikes of 3–12 m-thick intruding into the megacrystic granite were intercepted by several drill holes between 4250 and 3690 masl. These dikes are generally closely located to the Nazareth vein system and are cut by quartz-tourmaline vein-breccia bodies (stage I of the paragenetic sequence). The presence of lobed contacts with the megacrystic granite host, as well as K-feldspar megacrysts entrapped within the fine-grained granitic plug, strongly suggest commingling between these two granitic rocks. The dismembered fine-grained granitic plug has an equigranular texture containing millimeter-sized biotite in a quartz-feldspar groundmass with rare cordierite (Fig. 3C; Supplementary Fig. 1). QEMSCAN analysis of the least altered sample of fine-grained granitic plug yields 30.6% K-feldspar, 20.8% quartz, 23.5% plagioclase, 10.6% albite, 10.4% biotite, and <1% of accessory minerals including tourmaline, apatite, ilmenite, sphene, rutile, monazite, zircon, and pyrrhotite (Supplementary Fig. 1). Hydrothermal alteration minerals consist dominantly of muscovite, chlorite, and kaolinite identical to the megacrystic granite and the fine-grained granite.

(iv) *Medium-grained granite* is found as irregular enclaves (Fig. 2C) or dismembered dikes (Fig. 2G) in the megacrystic granite, mostly in the underground workings. This granitic rock is equivalent to the granodiorite described by Kontak and Clark (2002). The enclaves and dikes of medium-grained granite show lobed contacts without chilled margins and contain numerous partially resorbed K-feldspar phenocrysts from the megacrystic granite host (Fig. 2C-E), suggesting commingling of the two magmas before their solidification. The medium-grained granite is a mesocratic rock composed of millimeter-sized globular quartz crystals disseminated in a quartz-feldspar groundmass (Fig. 3D) containing rounded pinitized cordierite phenocrysts. The least altered medium-grained granite has a primary composition of 27.6% K-feldspar, 25.6% quartz, 14.6% plagioclase, 13.3% albite, 10.1% biotite, and < 1% of accessory minerals (apatite, ilmenite, sphene, rutile, zircon, monazite, pyrrhotite), as determined by QEMSCAN (Fig. 5B; Supplementary Fig. 1). Muscovite, chlorite, and kaolinite are the main alteration minerals (<8%) replacing the feldspars, biotite, and cordierite.

(v) *Tourmaline-bearing leucogranite*, initially described by Kontak and Clark (2002), occurs as a volumetrically minor plug in the northwestern part of the San Rafael stock (Fig. 1B), and locally as dikes in proximity to the Quenamari granite. Field relationships with the megacrystic granite are unclear, but the tourmaline-bearing leucogranite possibly intruded tardily into the granitic pluton. The tourmaline-bearing leucogranite is composed of millimeter-sized quartz (29.7%), albite (30.3%), K-feldspar (30.3%), tourmaline (1.5%), biotite (1.3%), and accessory minerals (<1%) including apatite, rutile, ilmenite, zircon, and monazite, as determined by QEMSCAN (Figs. 3E and 5C; Supplementary Fig. 1). Muscovite and kaolinite are the dominant alteration minerals (<7%) and partly replace the K-feldspar and albite phenocrysts.

(vi) *Porphyritic granite* is not exposed and was discovered in 2015 by diamond drilling at a depth of >500 m below surface in the Quenamari area (Fig. 1B-C). The porphyritic granite consists of a plug with approximate thickness of 100–400 m, striking north obliquely to the Nazareth vein system, and crosscutting the Quenamari pluton. The porphyritic granite appears to be the latest intrusion in the SRIC and is thought to postdate the main ore stage II, according to crosscutting relationships and overprinting on the cassiterite-bearing vein system. Locally, the porphyritic granite is cut by millimeter-thick veinlets of pyrite, fine-grained cassiterite, and Ag-bearing sulfosalts, as well as quartz-calcite-adularia veinlets, which are characteristic of the stages III and IV of the paragenetic sequence of the deposit, respectively (Kontak and Clark, 2002). These observations indicate that the porphyritic granite was emplaced temporally between the main Sn ore stage II and the polymetallic (Cu-Pb-Zn ± Ag-Sn-Bi) stages III and IV. The porphyritic granite is a leucocratic rock containing millimeter-sized phenocrysts of quartz and K-feldspar within a fine-grained quartz-feldspar±biotite groundmass (Fig. 3F). The K-feldspar and plagioclase phenocrysts are strongly altered, showing resorption textures, and are replaced by hydrothermal K-feldspar while biotite is almost completely replaced by muscovite or limonite (Supplementary Fig. 1). QEMSCAN analysis of the porphyritic granite reveals mineral abundances of 57.8–68.1% K-feldspar, 21.7–24.9% quartz, 2.6–3.7% albite, 3.3–9.6% muscovite, 0.3–1.7% biotite, 0.5–1.0% kaolinite, and < 1% accessory minerals including apatite, rutile, ilmenite, zircon, and monazite (Supplementary Fig. 1). The porphyritic granite is strongly hydrothermally altered as shown by the low contents of plagioclase and the elevated proportions of hydrothermal minerals (mainly K-feldspar, muscovite, calcite, kaolinite, and limonite).

(vii) *Lamprophyre* dikes and enclaves are observed in the underground workings (e.g., levels 3800 and 4200 masl) and are subordinately cropping out in the Quenamari area (Fig. 1). The dikes are 10–40 cm-wide, subvertical, and mostly cut the megacrystic granite and the fine-grained granite (Fig. 2D). Locally, lamprophyre enclaves, elongate and lobate in shapes, surrounded by mica-rich margins, are observed in the megacrystic granite and the medium-grained granite (Fig. 2E-F), supporting evidence for mingling between mafic melts and granitic magmas in the upper part of the pluton. The lamprophyres have a fine-grained texture and show highly variable mineral compositions consisting of 40.6–62.9% K-

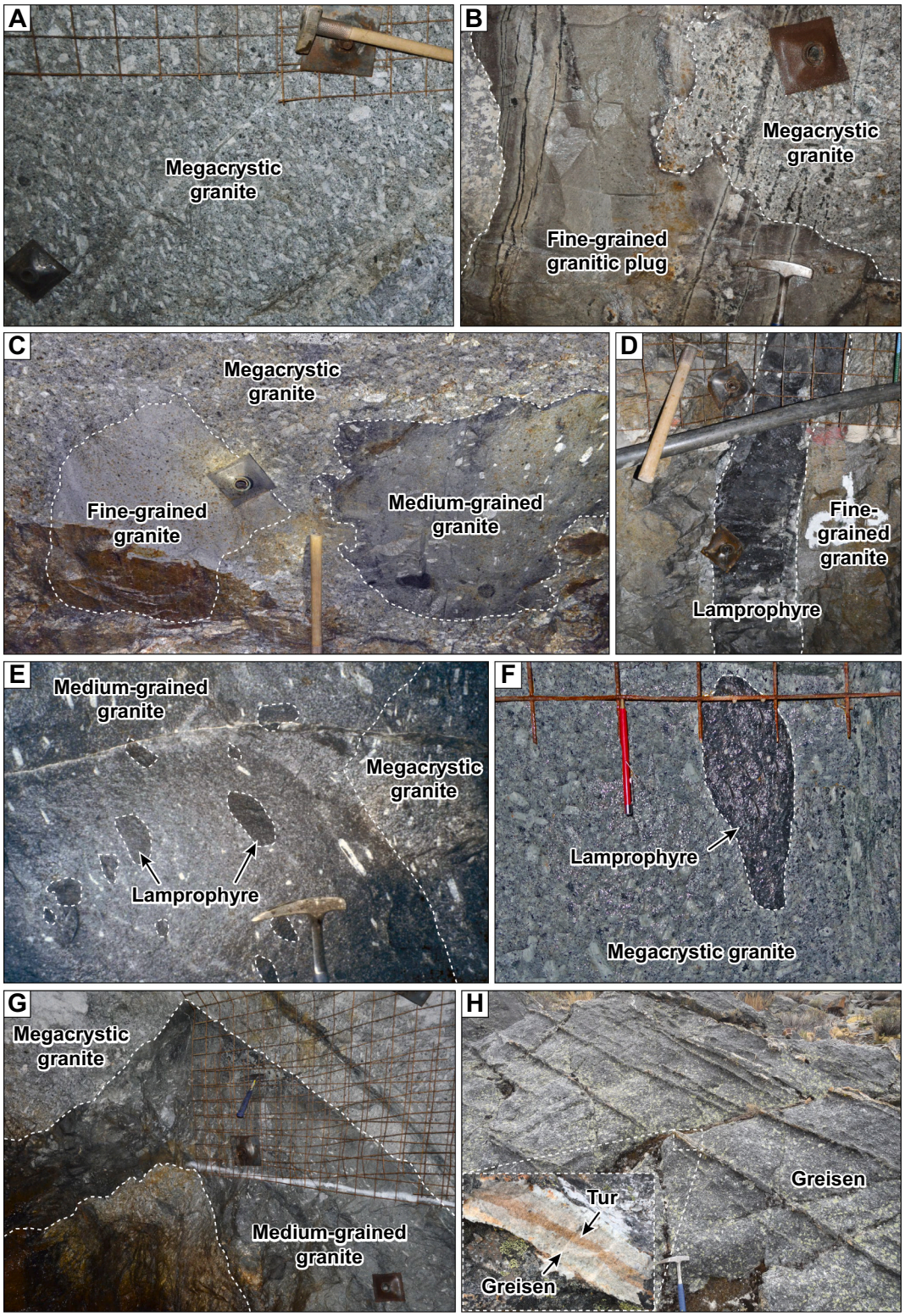

Fig. 2. Field relationships in the SRIC. A) Megacrystic biotite-cordierite-bearing granite containing centimeter-sized phenocrysts of K-feldspar (underground level 3800-m). B) Dismembered fine-grained granitic plug intruded in the megacrystic granite and showing mingling evidence (underground level 3800-m). Both intrusions are crosscut by subvertical hydrothermal quartz-tourmaline veins (stage I of the paragenetic sequence). C) Enclaves of fine-grained and medium-grained granites in the megacrystic granite showing mingling textures (underground level 3800-m). Note the presence of K-feldspar phenocrysts entrapped in the medium-grained granite as a result of mingling with the megacrystic granite. D) Subvertical dike of lamprophyre cutting the fine-grained granite (underground level 3800-m). E) Swarms of lamprophyre enclaves mingled with a large comagmatic enclave of medium-grained granite in the megacrystic granite (underground level 4200-m). F) Lobate enclave of lamprophyre in the megacrystic granite (underground level 3610-m). G) Dike of medium-grained granite partly dismembered into the megacrystic granite (underground level 3800-m). Note the undulous contacts of the dike, the absence of chilled margins, and the presence of partially resorbed K-feldspar phenocrysts in the medium-grained granite. H) Greisen-bordered veins of tourmaline (Tur) crosscutting the megacrystic granitic cupola at surface (Larancota, elevation 4926-m).

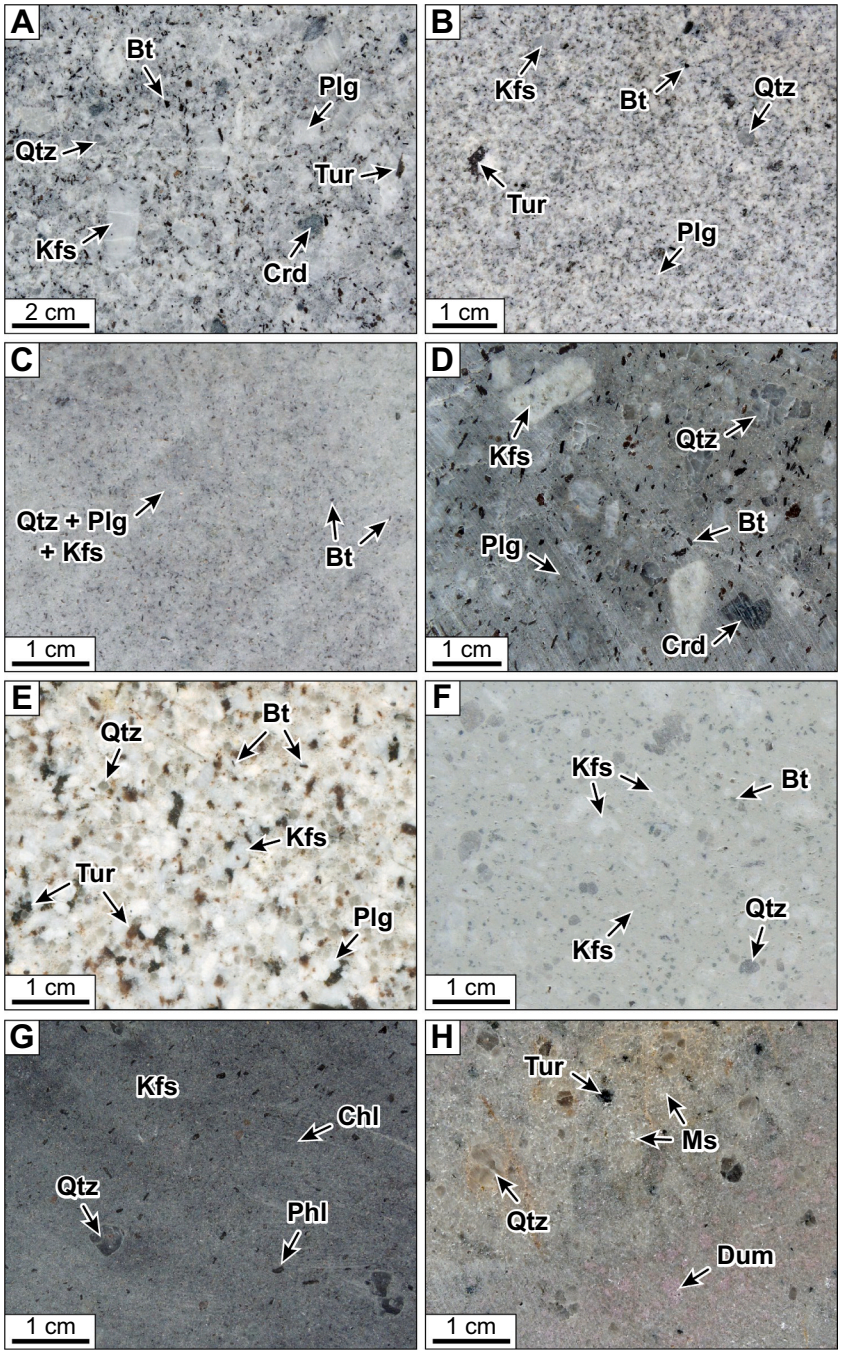

Fig. 3. Photographs of representative rock samples from the SRIC. A) Biotite-cordierite megacrystic granite composing the San Rafael pluton (sample SRG-38, level 3610-m). B) Fine-grained granite locally in contact with the San Rafael megacrystic granite (sample SRG-40, level 3610-m). C) Dismembered fine-grained granitic plug intrusive into the San Rafael megacrystic granite (sample SR-MH-38, level 3800-m). D) Medium-grained granite present as comagmatic enclave within the San Rafael megacrystic granite (sample SRG-16A, level 3800-m). E) Tourmaline-bearing leucogranite cropping out on the northwestern margin of the San Rafael granite (sample SRG-179, Larancota, elevation 4910-m). F) Porphyritic granite plug observed in drill core at Quenamari (sample SRG-73, drill-hole NAZ_002_15, depth 889-m). G) Lamprophyre dike cutting the San Rafael granitic stock (sample SRG-111, level 3800-m). H) Tourmaline and dumortierite-bearing greisen located in the upper part of the San Rafael pluton (sample SRG—133B, Larancota, elevation 4926-m). Abbreviations: Bt = biotite, Chl = chlorite, Crd = cordierite, Dum = dumortierite, Kfs = K-feldspar, Ms = muscovite, Phl = phlogopite, Plg = plagioclase, Qtz = quartz, Tur = tourmaline.

feldspar, 4.8–26.9% quartz, 5.6–18.2% phlogopite, 0.1–4.9% plagioclase (Ca-dominated), 2.2–3.9% albite, 0.4–15.9% actinolite, and 0.8–3.4% accessory minerals, including sphene, rutile, apatite, fluorite, ilmenite, zircon, and monazite (Fig. 3G; Supplementary Fig. 1). The lamprophyres are hydrothermally altered by chlorite (2.7–12.8%) and muscovite (0.1–3.5%) replacing selectively the micas and feldspars.

(viii) *Greisen* represents a volumetrically minor, altered portion of the southwestern tip of the San Rafael granitic cupola. It occurs at an elevation of >4800 masl as an elongated body extending approximately 600 m in NNW-SSE direction close to the contact with the metasedimentary host rocks (Fig. 1B). A continuous and gradual transition zone from the greisen to the megacrystic granite is observed in outcrops, suggesting that greisenization is a subsolidus alteration subsequent to the crystallization of the granitic intrusion. Locally, subvertical quartz-tourmaline sheeted veins crosscut the greisenized megacrystic granite (Fig. 2H). The greisen consists of a secondary quartz (49.9–58.5%) and coarse-grained muscovite (20.8–43.8%) assemblage, with variable amounts of dumortierite (0.65–19.8%) and tourmaline (0.24–18.6%; Fig. 3H, Supplementary Fig. 1). Dumortierite was identified by optical microscopy, SEM-EDS, X-ray diffraction, and Raman spectroscopy analyses (Supplementary Fig. 2).

4.2. Whole rock major and trace element compositions

Whole rock compositions of rocks from the SRIC are shown in Figs. 6–9 and the complete dataset ($n = 67$) is reported in Supplementary Table 1. The least altered granitic rocks have molar ratios $Al_2O_3/(CaO + Na_2O + K_2O) = 1.0–1.4$ and $Al_2O_3/(Na_2O + K_2O) = 1.3–1.7$ (Fig. 6A),

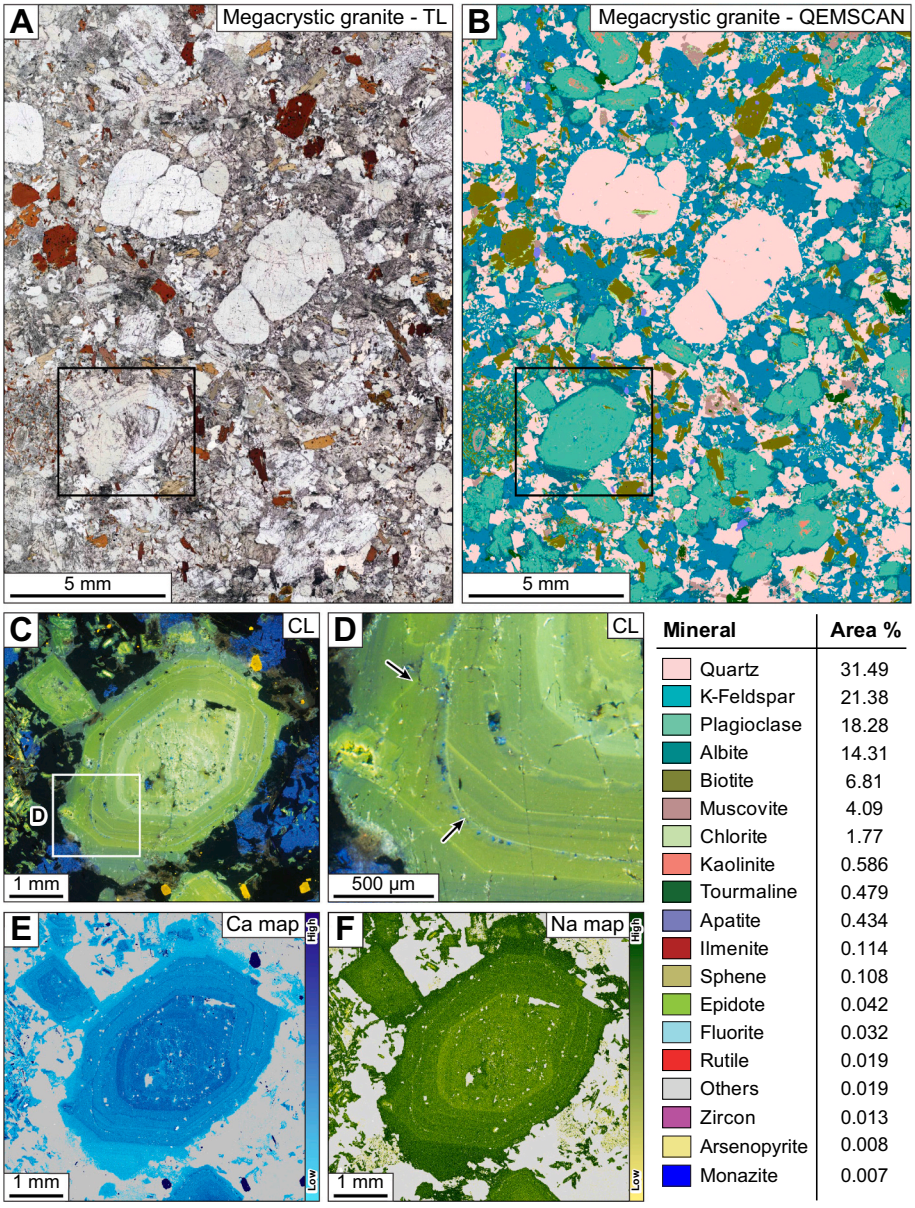

Fig. 4. Petrographic features of the megacrystic cordierite-biotite-bearing granite composing the SRIC. A) Plane polarized transmitted light photomicrograph and B) QEMSCAN false-color mineralogical map of a representative thin section (sample SRG-38, level 3610-m). C) Cold cathodoluminescence (CL) image of a plagioclase phenocryst showing primary zoning. The location of the crystal is shown by a black rectangle on images A) and B). D) Zoom on the primary zoning in plagioclase showing magmatic core with dissolution evidence (arrow) and albitic overgrowth. E-F) Ca and Na intensity maps of the same plagioclase phenocryst generated by QEMSCAN. The white color corresponds to pixels non-attributed to a mineral phase (mostly vugs).

falling into the peraluminous domain. In the B-A and P-Q diagrams (see Bonin et al., 2020 for description), the granitic rocks plot into the granite field and have low to highly peraluminous compositions, except for the tourmaline-bearing leucogranite that falls into the felsic peraluminous field (Fig. 6B-C). The granitic rocks plot at the limit between the high-K calc-alkaline and shoshonitic series (Fig. 6D) while they define a cluster straddling the boundaries of the granite, granodiorite, and quartz monzonite fields in the total alkali vs. silica diagram (Fig. 6E). The normative mineral compositions of all San Rafael granitic rocks plot into the field of monzogranites in the QAP ternary diagram (Fig. 6F). The main granitic rocks (megacrystic granite, fine-grained granite, dismembered fine-grained granitic plug, and medium-grained granite) have close SiO_2 contents (65.9–71.0 wt%) that correlate negatively with Al_2O_3 (14.6–16.2 wt%), Fe_2O_3 (1.7–3.6 wt%), MgO (0.7–1.9 wt%), CaO (0.7–2.0 wt%), and Na_2O (2.4–4.0 wt%; Fig. 7). Their trace element contents are similar, notably for Li (139–275 ppm), B (28–640 ppm), Ga (18–30 ppm), Rb (257–389 ppm), Sr (153–627 ppm), Y (10–33 ppm), Zr (100–371 ppm), Sn (3–40 ppm), Cs (18–251 ppm), Ba (404–2083 ppm) and REE (134–531 ppm; Supplementary Fig. 3), and show relative depletions in Ba, Sr and Ti, and relative enrichments in Cs, Rb, Pb and U when normalized to upper continental crust (UCC; Fig. 8A-C). These compositions are similar to granitic rocks of the Santo Domingo Sn deposit, located about 25 km west of San Rafael (Supplementary Table 1). Chondrite-normalized REE spectra of the main granites are similar with moderate $(La/Yb)_N$ ratios (13–52) and negative Eu anomalies ($(Eu/Eu^*)_N$ = 0.5–0.7; Fig. 9A-C). The tourmaline-bearing leucogranite defines the high-SiO_2 end (71.3–74.6 wt%) of the trend and has as such the lowermost contents of Al_2O_3 (14.6–15.2 wt%), Fe_2O_3 (1.0–1.7 wt%), MgO (0.2–0.6 wt%) and CaO (0.2–0.6 wt%) while the porphyritic granite has specifically low Na_2O (0.5–1.5 wt%) and high K_2O (6.5–8.0 wt%) contents (Fig. 7). Compared to the main granites, the tourmaline-bearing leucogranite and porphyritic granite have overlapping to higher contents of Li (189–604 ppm), B (71–683 ppm), Sn (17–45 ppm), Cs (136–445 ppm), Ga (30–35 ppm) and Rb (525–777 ppm), and lower contents of Ba (52–347 ppm), Sr (20–149 ppm), Zr (32–77 ppm), Y (5.8–11 ppm) and REE (35–84 ppm). They show comparable UCC-normalized trace element patterns to the main granites (Fig. 8D) but their chondrite-normalized REE spectra differ by lower $(La/Yb)_N$ ratios (5–24) and deeper negative to no Eu anomalies ($(Eu/Eu^*)_N$ = 0.3–0.5; Fig. 9D).

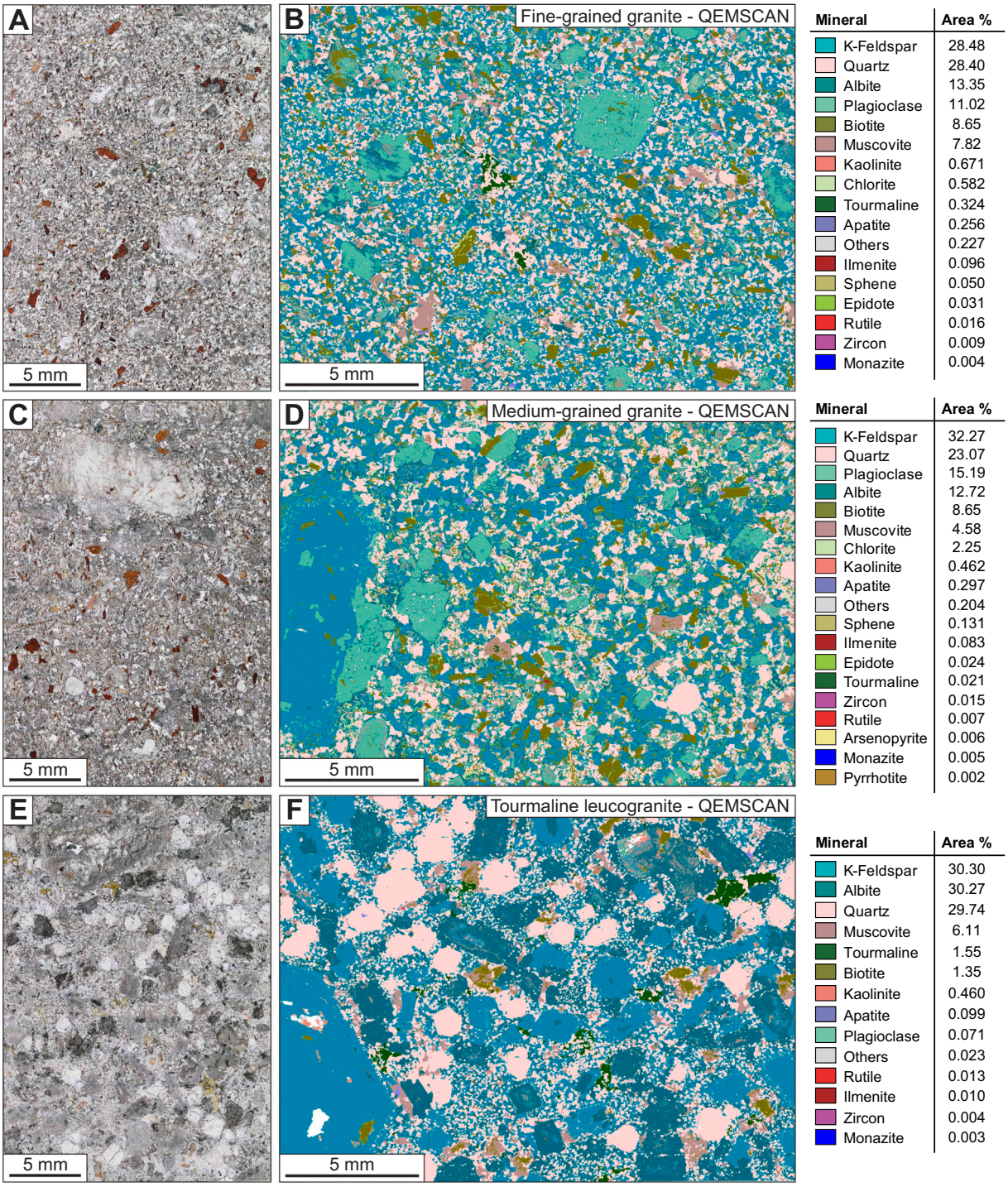

Fig. 5. Transmitted light photomicrographs and QEMSCAN false-color mineralogical maps showing petrographic features of the main San Rafael granite varieties. A-B) Fine-grained granite showing gradual contact with the megacrystic granite at surface (sample SRG-144, elevation 5042-m). C—D) Medium-grained granite present as comagmatic enclave in the megacrystic granite (sample SRG-48, drill core). E-F) Tourmaline-bearing leucogranite exposed on the northwestern margin of the San Rafael granite (sample SRG-179, elevation 4910-m). The white color corresponds to pixels non-attributed to a mineral phase (mostly vugs).

The lamprophyres are characterized by variable contents of SiO_2 (55.1–65.6 wt%), Fe_2O_3 (4.0–7.7 wt%), K_2O (3.8–7.1 wt%), MgO (3.5–7.8 wt%), CaO (1.2–5.0 wt%) and Na_2O (0.1–1.8 wt%; Fig. 7). They have high contents of Li (193–332 ppm), V (51–139 ppm), Cr (153–484 ppm), Ni (69–202 ppm), Cu (8.3–56 ppm), Zn (55–396 ppm), Rb (181–406 ppm), Sr (224–1267 ppm), Y (17–38 ppm), Zr (224–655 ppm), Nb (14–35 ppm), Cs (17–148 ppm), Ba (1316–4838 ppm) and REE (164–493 ppm). The trace element compositions of San Rafael lamprophyres are comparable to the ones of Miocene lamprophyres from the Eastern Altiplano and the Eastern Cordillera of southern Peru (Fig. 8E). Similarly, their chondrite-normalized REE spectra show moderate $(La/Yb)_N$ ratios (7.5–47) and negative Eu anomalies ($(Eu/Eu^*)_N$ = 0.7–1.0; Fig. 9E). Compared to the main granitic rocks, the Sandia metasedimentary rocks have lower SiO_2 (51.3–60 wt%), Na_2O (0.6–1.4 wt%) and CaO (0.2–0.5 wt%), and higher Al_2O_3 (19.8–25.4 wt %) and Fe_2O_3 (1.2–9.7 wt%). They show similar trace element contents

to the granite values including Li (158–381 ppm), B (108–722 ppm), Zr (148–172 ppm), Sr (83–143 ppm), Nb (16–20 ppm), Sn (4.8–38 ppm), Cs (30–421 ppm), REE (237–334 ppm) and Ta (1.3–1.4 ppm). This is also shown by their trace element and REE spectra comparable to the granitic rocks, including moderate $(La/Yb)_N$ ratios (6.2–8.4) and negative Eu anomalies ($(Eu/Eu^*)_N$ = 0.6–0.7; Figs. 8E and 9E). Only a few trace elements are markedly enriched in the Sandia metasedimentary rocks such as V (125–178 ppm), Cr (76–113 ppm), Ni (17–50 ppm), Zn (67–1056 ppm) and Y (43–64 ppm). Expectedly, greisenization of the San Rafael megacrystic granite results in high SiO_2 (73.9–76.9 wt%), low K_2O (2.7–3.1 wt%), and extremely low Na_2O (0.2–0.3 wt%) and CaO (0.2–0.3 wt%) contents. Relative to the main granites, the greisen shows higher B (571–3170 ppm) and Sn (35–49 ppm) contents, and lower Li (54–55 ppm), Ga (2–6 ppm), Sr (17–34 ppm), Y (3–6 ppm) and REE (12–34 ppm) contents. Greisenization results in distinct UCC-normalized trace element spectra (Fig. 8F) and chondrite-normalized REE patterns with lower $(La/Yb)_N$ ratios (2.9–7.2) and positive Eu anomalies ($(Eu/Eu^*)_N$ = 1.0–1.9; Fig. 9F).

4.3. Sr, Nd, and Pb isotopic compositions

The Sr, Nd, and Pb isotopic compositions of rocks from the SRIC are plotted in Fig. 10 and the full dataset is reported in Supplementary Table 2. The least altered megacrystic granite, fine-grained granite and the tourmaline-bearing leucogranite have similar ratios of $^{87}Sr/^{86}Sr_{(i)}$ (0.7170–0.7202, avg. = 0.7192 ± 0.0013) and $^{143}Nd/^{144}Nd_{(i)}$ (0.51210–51,214, avg. = 0.51213 ± 0.00001), which plot in a narrow cluster overlapping the field of Coastal and Western Cordillera intrusions. These $^{87}Sr/^{86}Sr_{(i)}$ values are consistent with previous data on the San Rafael and Quenamari granites (Kontak et al., 1987) and also fall in the compositional range of Bolivian Sn porphyries (Dietrich et al., 2000). These values overlap the Sr-Nd isotopic compositions of granitic rocks from the nearby Santo Domingo Sn deposit (Supplementary Table 2). The dismembered fine-grained granitic plug and the porphyritic granite have lower $^{87}Sr/^{86}Sr_{(i)}$ (0.7131–0.7149, avg. = 0.7140 ± 0.0013) and higher $^{87}Sr/^{86}Sr_{(i)}$ (0.7278–0.7294, avg. = 0.7286 ± 0.0012), respectively, than the other granitic rocks. The lamprophyres have more primitive compositions of $^{87}Sr/^{86}Sr_{(i)}$ (0.7087–0.7132, avg. = 0.7110 ± 0.0032) and $^{143}Nd/^{144}Nd_{(i)}$ (0.51236–0.51243, avg. = 0.51239 ± 0.00005) plotting close to the field of Miocene lamprophyres from the southern Peruvian Altiplano (Carlier et al., 2005). In comparison, the Sandia metasedimentary rocks have higher $^{87}Sr/^{86}Sr_{(i)}$ (0.7235–0.7311, avg. = 0.7276 ± 0.0030) and lower $^{143}Nd/^{144}Nd_{(i)}$ (0.51134–0.51366, avg. = 0.51206 ± 0.00094) ratios, which partly overlap the field of the Arequipa-Antafolla metamorphic basement. Altered granites show variable ratios of $^{87}Sr/^{86}Sr_{(i)}$ (0.7162–0.7294, avg. = 0.7224 ± 0.0048) and $^{143}Nd/^{144}Nd_{(i)}$ (0.51195–0.51227, avg. = 0.51209 ± 0.00009) relative to their least altered equivalents.

The Pb isotope compositions of the least altered San Rafael granites are homogeneous with $^{206}Pb/^{204}Pb_{(i)}$, $^{207}Pb/^{204}Pb_{(i)}$, and $^{208}Pb/^{204}Pb_{(i)}$ ratios falling in the range of 18.58–18.88 (avg = 18.73 ± 0.03), 15.68–15.69 (avg = 15.69 ± 0.01), and 38.91–38.97 (avg = 38.94 ± 0.02), respectively. These values are consistent with the Pb isotope compositions of the San Rafael-Quenamari ores, as well as other Sn-W ± Cu-Zn-Pb-Ag ore deposits from the Eastern Cordillera of Peru and Bolivia (Kamenov et al., 2002; Kontak et al., 1990b; Macfarlane et al., 1990). These Pb isotope values are also similar to the compositions of granitic rocks from the nearby Santo Domingo Sn deposit (Supplementary Table 2). In the $^{206}Pb/^{204}Pb$ vs. $^{207}Pb/^{204}Pb$ diagram, the Pb isotopic ratios of the granites plot along the upper crust curve of Zartman and Doe (1981) and overlap the field of Coastal and Western Cordillera intrusions. The lamprophyres have lower $^{206}Pb/^{204}Pb_{(i)}$ values (18.27–18.52) but similar $^{207}Pb/^{204}Pb_{(i)}$ (15.67) and $^{208}Pb/^{204}Pb_{(i)}$ (39.04) ratios compared to the granites. The Sandia metasedimentary rocks have $^{206}Pb/^{204}Pb_{(i)}$ (18.32–18.86, avg. = 18.58 ± 0.24) and $^{207}Pb/^{204}Pb_{(i)}$ (15.63–15.68, avg. = 15.67 ± 0.02) ratios partly overlapping the values of granites and lamprophyres while having higher $^{208}Pb/^{204}Pb_{(i)}$ ratios (39.48–39.98, avg. = 39.67 ± 0.20). Altered granites show variable initial Pb isotope ratios ($^{206}Pb/^{204}Pb_{(i)}$ = 17.84–18.81, $^{207}Pb/^{204}Pb_{(i)}$ = 15.64–15.69, and $^{208}Pb/^{204}Pb_{(i)}$ = 38.93–39.20) compared to the least altered precursors.

4.4. U—Pb dating and trace element composition of zircon

Five representative samples of megacrystic granite, fine-grained granitic plug, medium-grained granite, porphyritic granite, and lamprophyre dike were selected for U—Pb zircon dating. Results of U—Pb analyses are shown in Fig. 11 and the complete dataset is reported in Supplementary Table 3. In all investigated samples, the zircons are euhedral with prismatic shapes, locally sub-rounded terminations, and range in length from 100–400 μm with aspect ratios between 2 and 4. The largest grains (>250 μm) are found only in the megacrystic granite and lamprophyre. SEM-CL imaging of zircon reveals that some grains are characterized by homogeneous, bright-CL cores with well-defined crystal shapes, surrounded by CL-darker rims showing oscillatory zoning parallel to the growth zones of the core, which is indicative of crystallization from the host granitic magma (Fig. 11; Supplementary Fig. 4). In other grains, the cores show either brighter or darker CL response, as well as weaker zoning that may be truncated by oscillatory zoned rims, which probably corresponds to inherited zircons. Fifty-six U—Pb analyses were carried out on twenty-five zircon grains from the megacrystic granite (sample SRG-38). Fourteen analyses allowed calculating a Concordia date of 24.03 ± 0.25 Ma (2σ, MSWD = 2.6) identical within uncertainty to the weighted mean $^{206}Pb/^{238}U$ date of 24.02 ± 0.25 Ma (2σ, MSWD = 0.84; Fig. 11A). Fifteen zircon grains from the dismembered fine-grained granitic plug (sample SRG-89) yielded a Concordia date of 24.17 ± 0.26 Ma (2σ, MSWD = 1.2) and a weighted mean $^{206}Pb/^{238}U$ date of 24.17 ± 0.28 Ma (2σ, MSWD = 1.5; Fig. 11B) from eight U—Pb analyses out of thirty-four in total. Sixteen out of thirty-two U—Pb analyses performed on seventeen oscillatory zoned zircon grains from the medium-grained granite (sample SRG-134) yielded a Concordia date of 24.27 ± 0.25 Ma (2σ, MSWD = 0.83) and a weighted mean $^{206}Pb/^{238}U$ date of 24.26 ± 0.26 Ma (2σ, MSWD = 1.5; Fig. 11C). Nine oscillatory zoned zircon grains from the lamprophyre (sample SRG-18) yielded a Concordia date of 23.80 ± 0.27 Ma (2σ, MSWD = 2.2), consistent with a weighted mean $^{206}Pb/^{238}U$ date of 23.79 ± 0.27 Ma (2σ, MSWD = 1.1; Fig. 11D) from four U—Pb spot analyses out of sixteen in total. Eighteen U—Pb analyses were performed on twenty-two zoned zircon grains from the porphyritic granite (sample SRG-73), but no concordant zircon age could be obtained. Histogram and probability density distribution of $^{206}Pb/^{238}U$ dates of all concordant inherited zircons (n = 50) show three main age groups (Fig. 12): (i) a dominant Triassic population at 200–250 Ma (n = 34) with a major peak at 220–235 Ma; (ii) a lower Cambrian population at 510–550 Ma (n = 8); and (iii) an upper Cambrian to Lower Ordovician population at 460–490 Ma (n = 4).

Trace element compositions of non-inherited zircons are shown in Figs. 13 and 14 and the complete dataset is reported in Supplementary Table 4. All zircons have similar chondrite-normalized patterns with moderate contents of REE (530–3760 ppm) and Y (740–5352 ppm), low $(La/Yb)_N$ ratios (<0.01), positive Ce anomalies ($(Ce/Ce^*)_N$ = 1.2–49), and negative Eu anomalies ($(Eu/Eu^*)_N$ = 0.04–0.17; Fig. 13). The concentrations of U (375–18,760 ppm) and Th (34–3100 ppm) are variable

with Th/U ratios varying from 0.01 to 0.94, mostly in the range of 0.1–0.6. Except P (176–2880 ppm) and Hf (7990–17,710 ppm), other trace elements have low concentrations including Li (0.01–3.2 ppm), B (0.01–3.9 ppm), Al (0.3–258 ppm), Ti (1.9–23.4 ppm), Nb (0.5–24.2 ppm), Sn (0.2–1.7 ppm), and Ta (0.4–15.0 ppm). Trace element variations in zircon are characterized by decreasing ratios of Th/U (0.94–0.01), Nb/Ta (3.39–0.53), Zr/Hf (54–28) and $(Sm/La)_N$ (930–99) with increasing $(Yb/Gd)_N$ ratios (6.6–91.9; Fig. 14). All zircons show overlapping trace element compositions, but the high-$(Yb/Gd)_N$ part of the trend is mostly defined by zircons from the megacrystic granite. Crystallization temperatures were calculated using the Ti-in-zircon thermometer of Ferry and Watson (2007), corrected for $a(SiO_2) = 1$ and $a(TiO_2) = 0.7$, to reflect the presence of magmatic quartz and accessory ilmenite (Claiborne et al., 2010; Hayden and Watson, 2007).

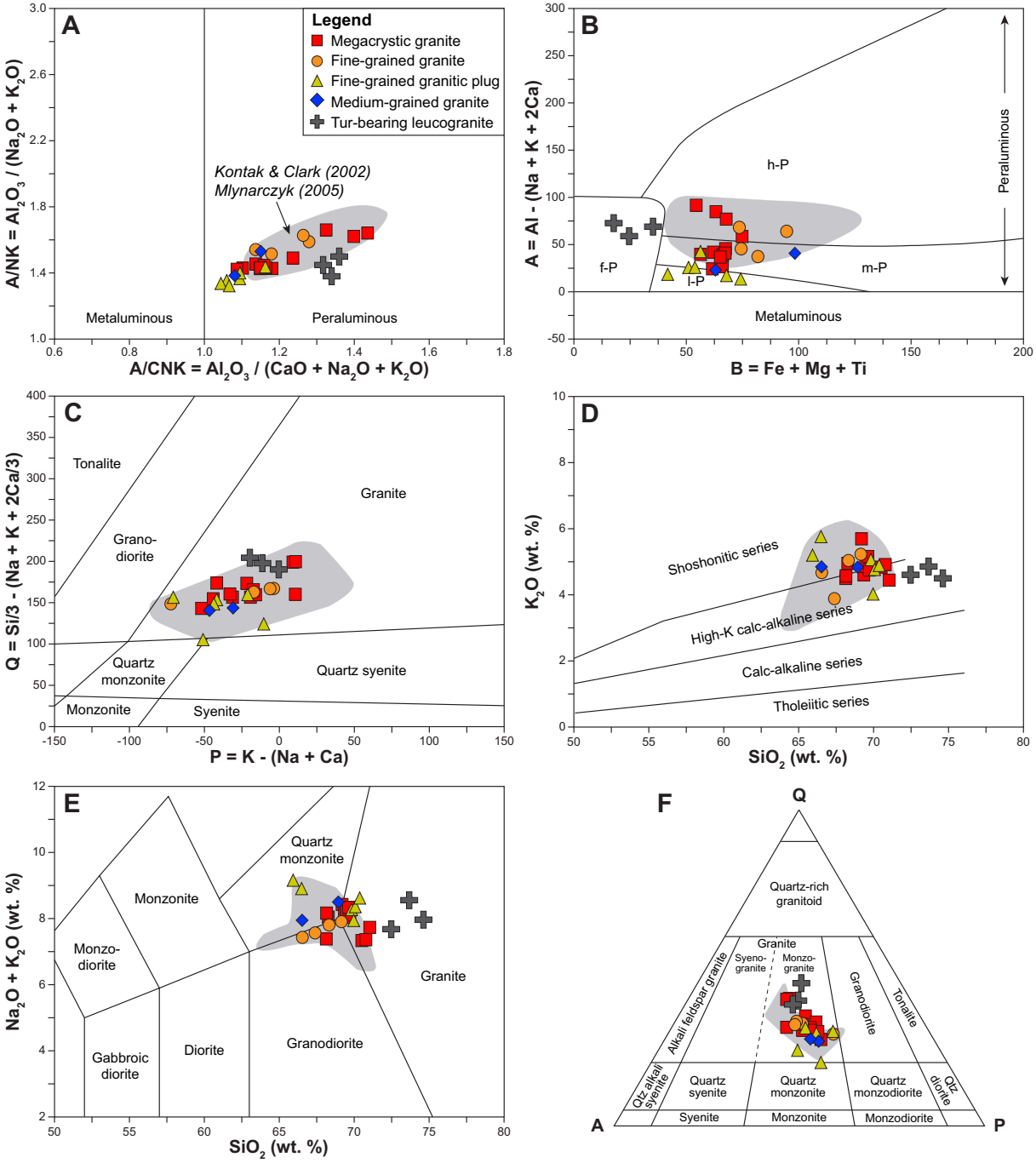

Fig. 6. Classification geochemical diagrams for the least altered granitic rocks from the SRIC. A) Alumina saturation diagram representing the molar ratio A/NK = $Al_2O_3/(Na_2O + K_2O)$ as function of the molar ratio A/CNK = $Al_2O_3/(CaO + Na_2O + K_2O)$. B) B-A diagram representing the differentiation index B = Fe + Mg + Ti as function of the peraluminous index A = Al-(Na + K + 2Ca) expressed in millications. The subdivision of the peraluminous domains corresponds to: low peraluminous (l-P), moderately peraluminous (m-P), highly peraluminous (h-P), and felsic peraluminous (f-P). C) P-Q diagram representing the relative proportion of feldspars P = K - (Na + Ca) as function of the quartz content Q = Si/3 - (Na + K + 2Ca/3) expressed in millications. D) K_2O vs. SiO_2 diagram showing the main magmatic series. E) Total alkali-silica diagram representing the $Na_2O + K_2O$ vs. SiO_2 contents. F) QAP modal classification diagram generated from the calculated CIPW normative mineralogical compositions. In all diagrams, the light grey field represent data for the least altered San Rafael megacrystic granite compiled from Kontak and Clark (2002) and Mlynarczyk (2005).

Temperatures calculated for zircons from the main granite varieties yield comparable values ranging from 638° to 840 °C (avg = 759 ± 49 °C; Fig. 14F and Supplementary Table 4).

5. Discussion

5.1. Petrogenetic constraints on the origin of the SRIC

The main granitic rocks of the SRIC (megacrystic granite, fine-grained granite, dismembered fine-grained granitic plug, and medium-grained granite) are overall characterized by similar mineralogical and geochemical compositions with variable textures. All the least altered San Rafael granites contain abundant quartz, K-feldspar, plagioclase, and biotite as primary igneous minerals with minor amounts of peraluminous mineral phases like cordierite or tourmaline in variable proportions (Figs. 3–5; Supplementary Fig. 1). From a geochemical perspective, the main San Rafael granites have moderately fractionated peraluminous compositions, relatively high Zr/Hf (31–35) and Nb/Ta (4–8) ratios (Supplementary Fig. 5), moderate enrichments in incompatible elements (Li, B, Ga, Rb, Sn, Cs, Th, and U), moderate $(La/Yb)_N$ ratios (13–52), and moderately pronounced negative Eu anomalies ($(Eu/Eu^*)_N$ = 0.5–0.7; Figs. 6–9). They also have trace element compositions close to the Sandia metasedimentary rocks (Figs. 8 and 9) and show strongly crustal Sr, Nd, and Pb isotopic signatures (Fig. 10), suggesting that the parental granitic melts must have a source component similar to the Paleozoic metasedimentary rocks occurring in the region. Zircons from the San Rafael granites show a fractionated pattern with positive Ce anomalies and negative Eu anomalies, typical for granitoids (Breiter et al., 2014; Gao et al., 2016; Pettke et al., 2005), while their relatively high Zr/Hf ratios (28–54) indicate a moderate fractionation degree of the granitic melt (Breiter et al., 2014). Similar decreasing trends of the Th/U, Nb/Ta, and Zr/Hf ratios, and the Ti content in zircon with increasing $(Yb/Gd)_N$ ratio are indicative of progressive crystal fractionation of the granitic melt (Buret et al., 2016; Chelle-Michou

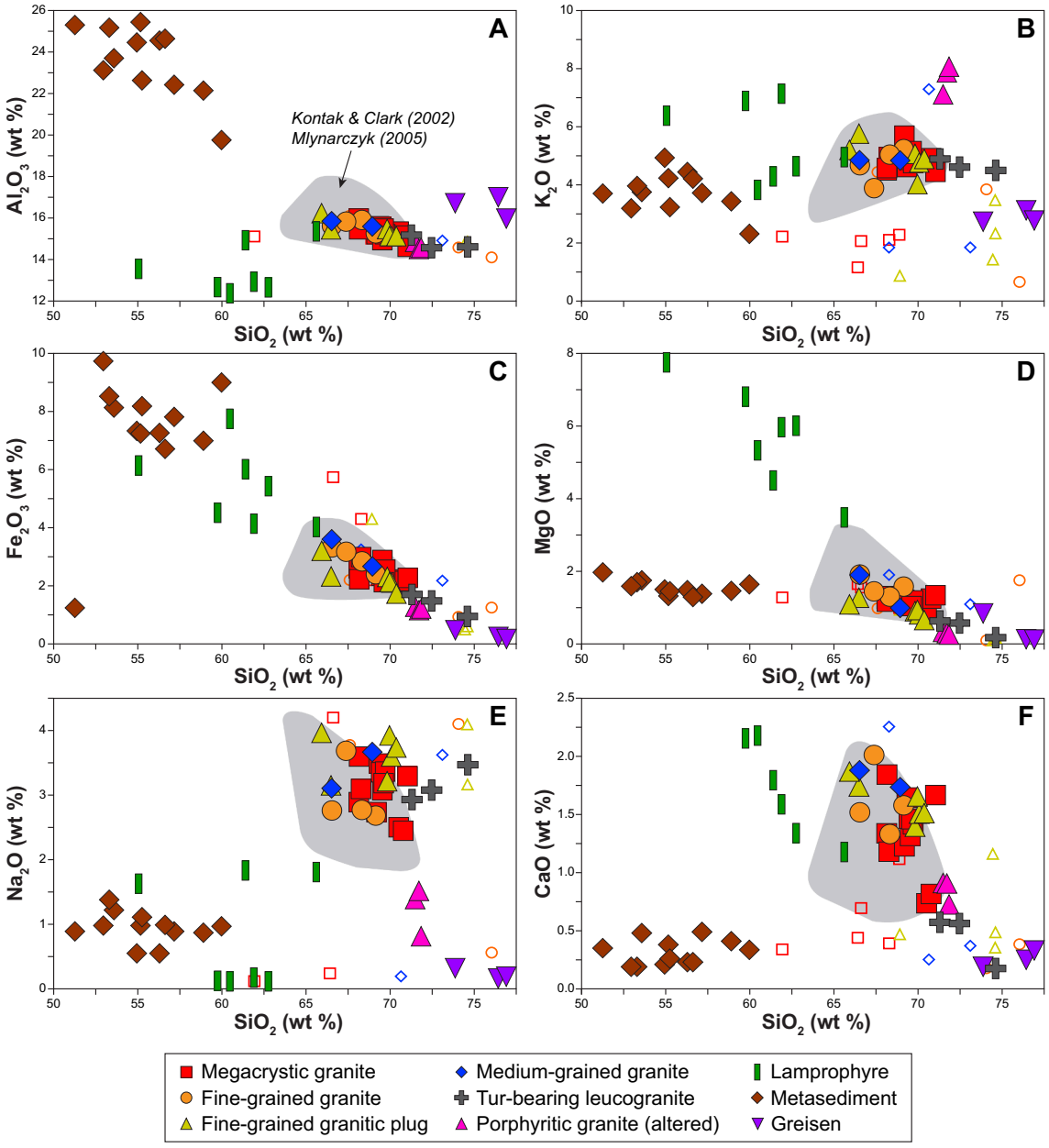

Fig. 7. Major element compositions of rocks from the SRIC. Filled and open symbols represent least altered and strongly altered samples, respectively. The light grey field represent data for the least altered San Rafael megacrystic granite compiled from Kontak and Clark (2002) and Mlynarczyk (2005).

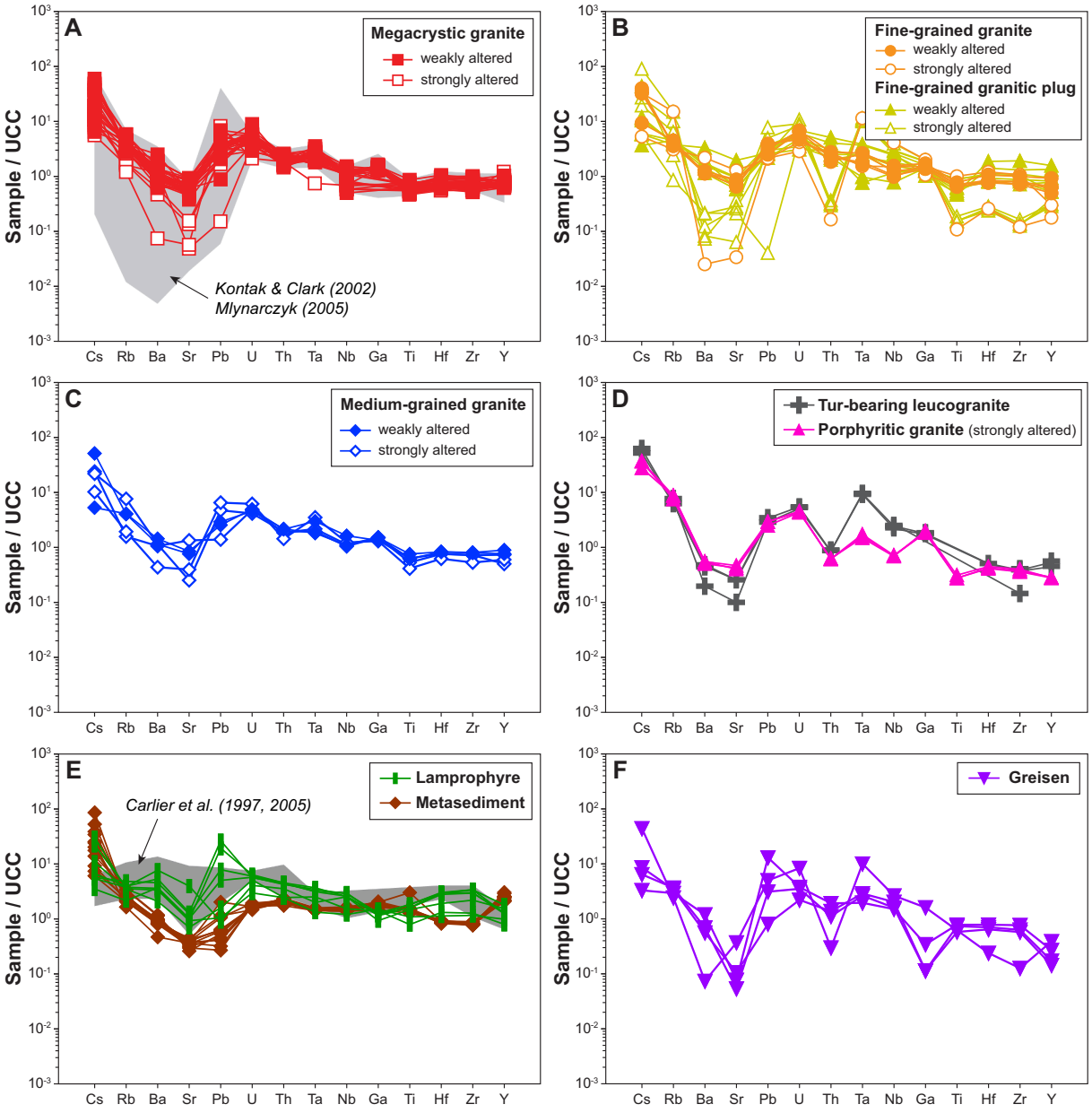

Fig. 8. Trace element compositions of rocks from the SRIC normalized to upper continental crust (UCC of Rudnick and Gao, 2014). The light grey field represent data for the least altered San Rafael megacrystic granite compiled from Kontak and Clark (2002) and Mlynarczyk (2005). The dark grey field correspond to Miocene lamprophyres from the Eastern Altiplano and the Eastern Cordillera of southern Peru (Carlier et al., 1997, 2005).

et al., 2014; Wotzlaw et al., 2013). The low $(Ce/Ce^*)_N$ and $(Eu/Eu^*)_N$ values of zircons from the San Rafael granites suggest a reduced character of the magmas (Trail et al., 2012), in accordance with the presence of ilmenite. Using the calibration of Trail et al. (2012) for a peraluminous melt composition (molar ratio Al/(Na + K) = 1.25), San Rafael zircons would have crystallized at $\Delta NNO = -4 \pm 1$ for temperatures of 800 °C. This is consistent with estimations using the oxybarometry calibration of Loucks et al. (2020) that gives $\Delta FMQ = -4 \pm 2$ on average and $\log fO_2 = -20 \pm 2$ for Ti-in-zircon temperatures of ca. 760 °C. The fractionation of plagioclase and accessory phases such as monazite and apatite prior or during zircon crystallization may have also influenced the zircon Ce—Eu anomalies (Deering and Bachmann, 2010; Hoskin and Schaltegger, 2003). This possibly contributed to lower the $(Ce/Ce^*)_N$ and $(Eu/Eu^*)_N$ values of the San Rafael zircons, implying that the estimate of $\log fO_2 \approx -20$ should be considered as a minimum.

These mineralogical and geochemical characteristics allow classifying the San Rafael granites as part of the cordierite-bearing peraluminous granitoids (CPG in the nomenclature of Barbarin, 1999), which correspond to the original S-type granites, as defined in the Lachlan Fold Belt of Australia (Chappell and White, 1992). Although there is little argument against the origin of S-type granitoids through biotite-breakdown melting of metasedimentary rocks, the chemical variations in both major and trace elements of CPG remain controversial. The bulk composition of these rocks cannot be reproduced by phase equilibrium modelling, even with Ca-, Fe-rich pelitic protoliths (Mayne et al., 2020), and must be explained by two possible, not mutually exclusive scenarios: (i) entrainment of restitic or peritectic mineral assemblages, and (ii) mixing with coexisting, mantle-derived mafic melts (Bonin et al., 2020; Farina et al., 2012; Stevens et al., 2007). One striking feature of the SRIC is the presence of numerous comagmatic enclaves of granites and subordinate lamprophyres, which is unambiguous evidence for multiple injection and mingling of several types of coexisting felsic

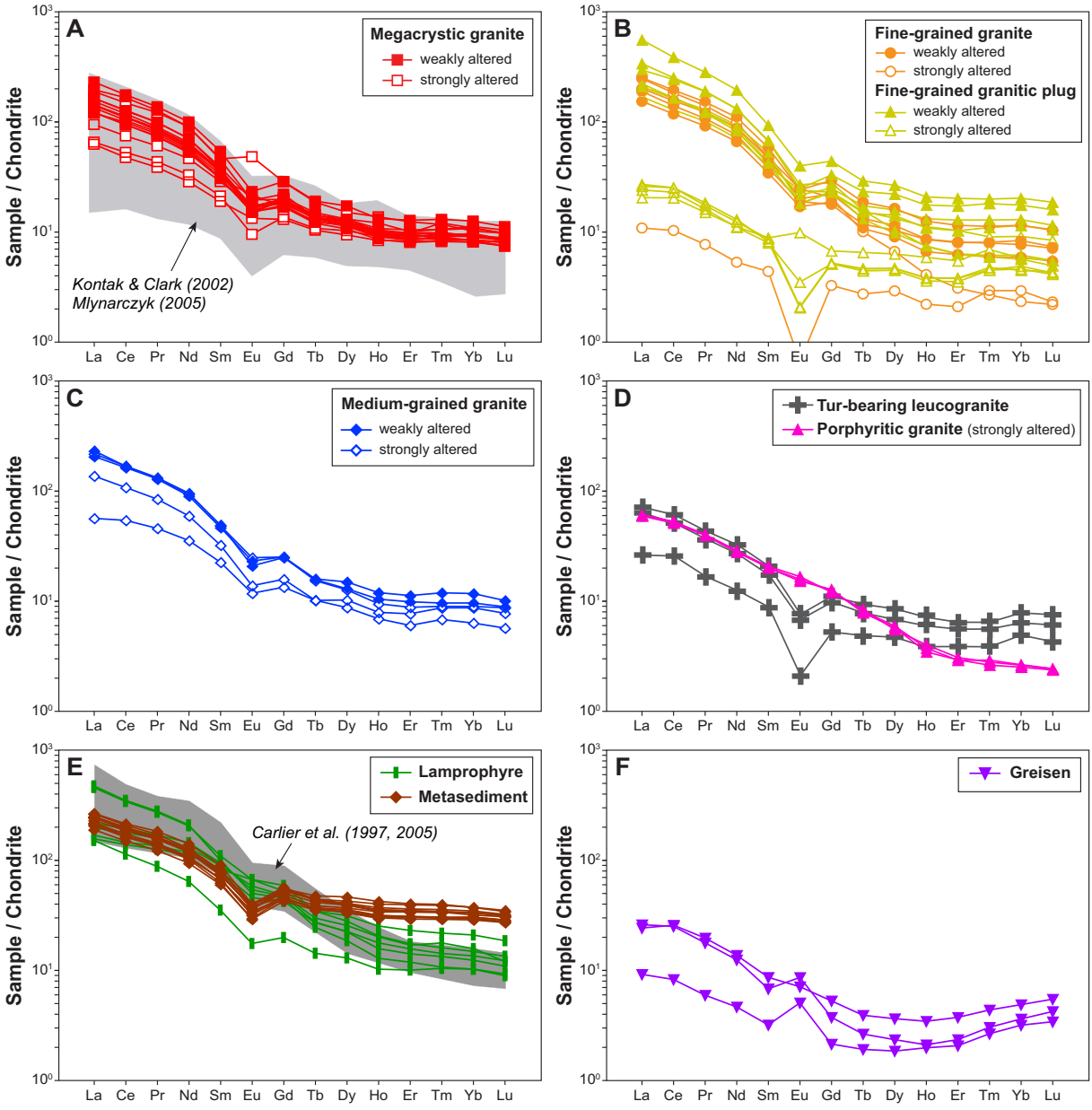

Fig. 9. Rare earth element compositions of rocks from the SRIC normalized to chondrite values of McDonough and Sun (1995). The light grey field represent data for the least altered San Rafael megacrystic granite compiled from Kontak and Clark (2002) and Mlynarczyk (2005). The dark grey field correspond to Miocene lamprophyres from the Eastern Altiplano and the Eastern Cordillera of southern Peru (Carlier et al., 1997, 2005).

and mafic magmas in a common magma reservoir. Additional evidence of magma mingling/mixing is provided by the partially resorbed K-feldspar phenocrysts of the megacrystic granite host present in some mafic and granite enclaves (Figs. 2–4), as well as the irregularly shaped and embayed morphology of quartz phenocrysts (Figs. 4 and 5; Supplementary Fig. 1). The San Rafael lamprophyres have high contents of lithophile elements (Li, Rb, Cs, Sn, W) while having more primitive Sr—Nd isotopic compositions (Fig. 10A), suggesting that they were derived from metasomatized subcontinental lithospheric mantle and were contaminated by crustal assimilation and/or mixing with granitic magmas (Abdelfadil et al., 2013; Carlier et al., 2005). Potassic and ultrapotassic lamprophyres of late Oligocene to early Miocene age (ca. 22–26 Ma) are documented in the Eastern Cordillera of southern Peru and are interpreted to result from the mixing between lamproitic and monzogranitic magmas (Carlier et al., 1997, 2005; Sandeman et al., 1997; Sandeman and Clark, 2003). The relatively high contents of Fe_2O_3 (1.7–3.6 wt%), K_2O (3.9–5.8 wt%), Ba (404–2083 ppm), Cr (19–72 ppm), Ni (4.7–27 ppm), and Cu (4.9–62 ppm) of the main San Rafael granite suite are similar to mafic S-type CPG from the Lachlan Fold Belt (Chappell and White, 1992). This would suggest, therefore, that the SRIC includes a component of magma mixing with coexisting mantle-derived mafic melts, which are possibly defined by potassic-ultrapotassic lamproite endmembers of the South Peruvian Potassic Province (Carlier et al., 1997, 2005).

5.2. *Regional geodynamic setting of the SRIC*

The SRIC is part of the upper Oligocene – lower Miocene (ca. 28–22 Ma) Picotani Group, confined to the Precordillera de Carabaya and comprising a suite of intrusive and volcanic units ranging in composition from subaluminous to peraluminous rhyolites, through metaluminous to subaluminous, medium- to high-K calc-alkaline and shoshonitic

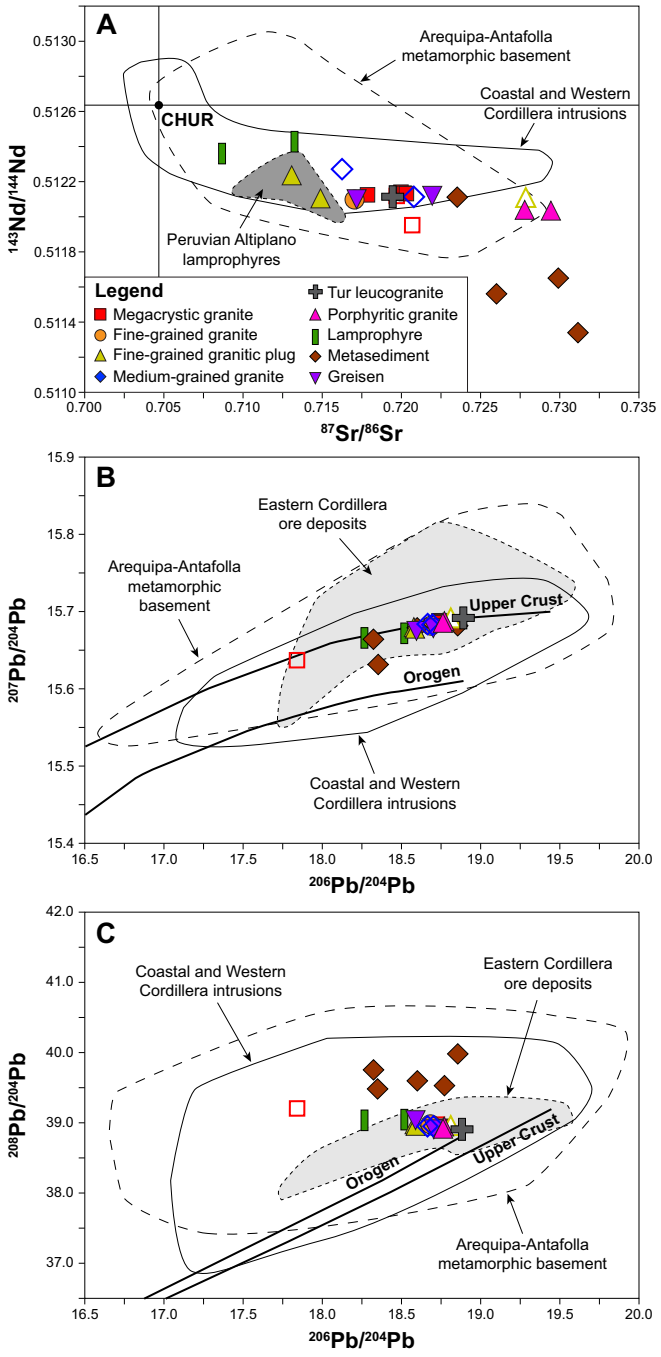

Fig. 10. Initial Sr, Nd, and Pb isotopic compositions of rocks from the SRIC and host rocks compared to the main crustal segments of the Central Andes compiled from the CAnDB database (Georg-August University of Göttingen, Germany: http://www.uni-geochem.gwdg.de/en/andes-database/andes-database). Filled and open symbols represent least altered and strongly altered samples, respectively. The dark grey field corresponds to Miocene lamprophyres from the southern Peruvian Altiplano (Carlier et al., 2005). The light grey field includes ore deposits from the Eastern Cordillera of Peru and Bolivia (Kamenov et al., 2002; Kontak et al., 1990b; Macfarlane et al., 1990). Isotopic ratios were corrected for an age of 25 Ma. Error bars are smaller than symbol sizes. Upper crust and orogen evolution curves are from Zartman and Doe (1981).

andesites and basalts, to ultrapotassic lamproites and lamprophyres (Carlier et al., 1997, 2005; Kontak and Clark, 1997; Sandeman et al., 1995, 1997; Sandeman and Clark, 2003, 2004). A characteristic feature of the Picotani Group is the quasi-pervasive evidence for extensive mixing of felsic and mafic magmas (Carlier et al., 1997, 2005; Clark and Kontak, 2004; Kontak and Clark, 1997; Sandeman and Clark, 2003, 2004). The Picotani Group constitutes the northernmost transect of the Central Andean Inner Arc, as defined by Clark et al. (1990), together with the contemporaneous, but petrogenetically distinct potassic-ultrapotassic magmatism (ca. 30–26 Ma; Carlier et al., 2005) in the contiguous Western Altiplano and the overlying Miocene (ca. 18–5 Ma) Quenamari Group of the Crucero Supergroup (Sandeman et al., 1997). The ultrapotassic associations of the Quenamari Group record partial melting of variably metasomatized lithospheric peridotites, dominated in southeast Peru by Archean-Paleoproterozoic, carbon- and phlogopite-bearing harzburgites, while the associated shoshonitic magmas were plausibly derived from asthenospheric peridotites with depleted mantle signatures (Carlier et al., 2005). The Central Andean Inner Arc magmatism is thought to be located at the inherited basement weakness zone constituted by the boundary between the Arequipa and Amazonia cratonic blocks (Ramos, 2018).

Termination of the Inner Arc magmatism in the Eastern Cordillera at ca. 22 Ma was accompanied by crustal thickening and uplift because of thermal weakening and ductile shortening of the lower orogenic crust during the early Miocene (Sandeman et al., 1995). Recent estimates of late Cenozoic surface uplift across the Peruvian Central Andes indicate that paleoelevation was about 2500 masl in the Eastern Cordillera during the late Oligocene (ca. 25 Ma) and then was slowly elevated 1.5–2 km between 25 and 10 Ma at a rate consistent with crustal shortening (Sundell et al., 2019). Emplacement of the upper Oligocene - lower Miocene Picotani Group, of which the SRIC is part, is bracketed temporally by two episodes of orogen-wide surface uplift and pediplanation, at ca. 32 Ma and 20 Ma, respectively, with the latter accompanying the initiation of the Quenamari Group (Quang et al., 2005; Sandeman et al., 1997). The uplift of the Eastern Cordillera during the late Oligocene - early Miocene suggests that the continental crust in this segment of the Central Andes was much thinner than the present-day crustal thickness (ca. 50–60 km; Ryan et al., 2016). The SRIC and its associated mineralization were therefore emplaced during major regional surface uplift and erosion attending progressive crustal thickening.

Following ca. 20 Ma of magmatic quiescence in this immediate orogenic transect, ascribed by Sandeman et al. (1995) to slab flattening in the Eocene, the Main Arc was reborn across a width of 200 km, with voluminous shoshonitic volcanism of the Tacaza Group at ca. 30-24 Ma (Mamani et al., 2010) along the inner margin of the Eastern Cordillera. This was followed at 25 Ma by major rhyolitic ignimbrite eruption further to the southwest (Quang et al., 2005). The quasi-instantaneous resumption of magmatic activity across a total orogenic width of ca. 400 km was interpreted by Sandeman et al. (1995) as resulting from slab breakoff and detachment at ca. 30 Ma, thus inducing major mantle upwelling beneath the Altiplano and anomalous asthenospheric heat flow, which generated voluminous high-K mafic magmas of the Tacaza arc. An alternative model of arc back-migration caused by slab steepening was proposed by Mamani et al. (2010) as a mechanism for mantle upwelling and decompression melting during the interval 30–24 Ma. Thus, the San Rafael deposit formed precisely at the continentward extremity of a ca. 400 km wide zone of active magmatism and hydrothermal activity, extending to within 75 km of the present coastline. We infer that the formation of the SRIC is the consequence of mantle-derived mafic melts injected into a relatively thinner orogenic crust resulting in high-temperature and low-pressure anatexis of predominantly semi-pelitic metasedimentary rocks through biotite dehydration melting.

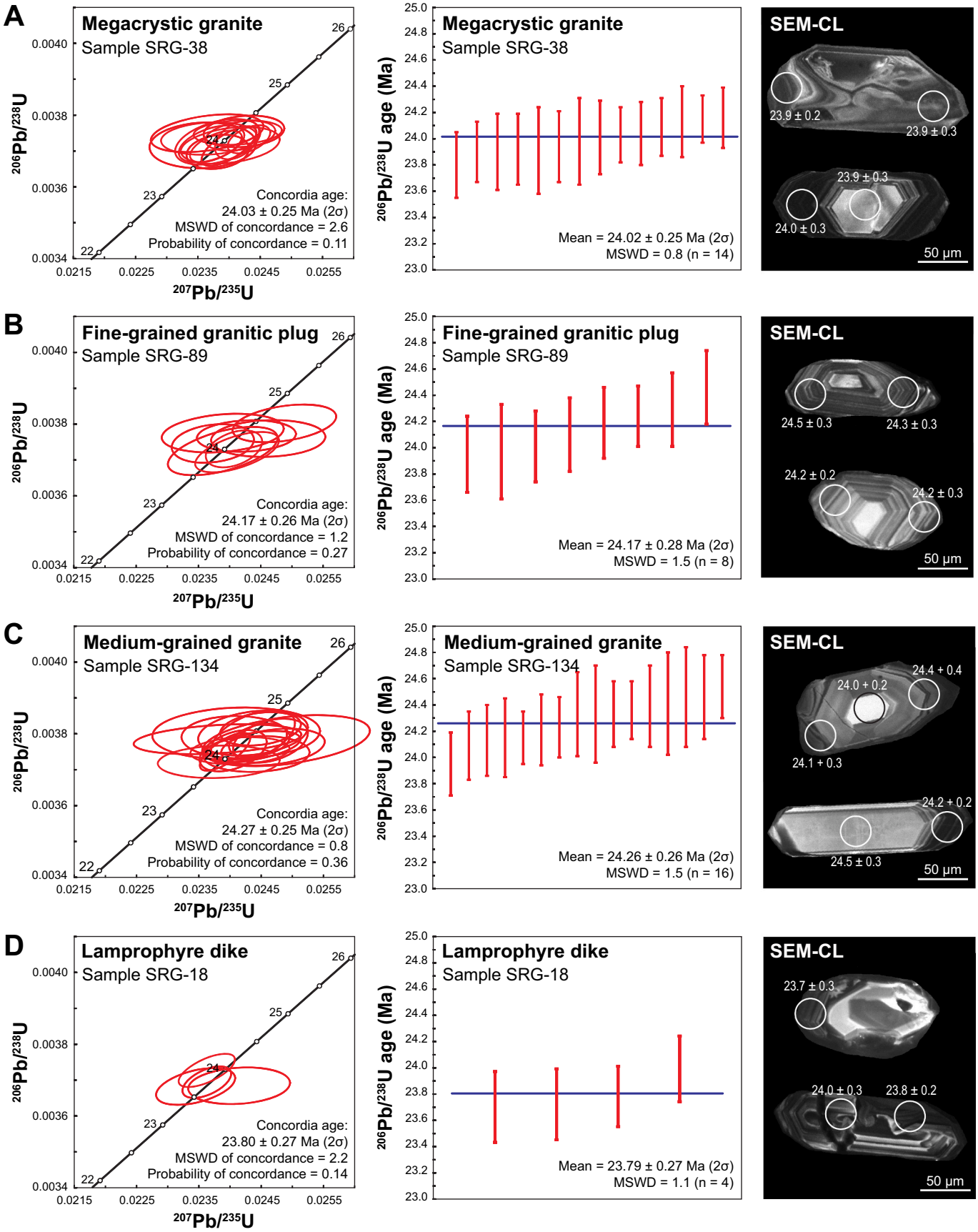

Fig. 11. Concordia diagrams and weighted mean $^{206}Pb/^{238}U$ ages of magmatic zircons from the SRIC. Data-point error ellipses and symbols are 2σ. Scanning electron microscopy - cathodoluminescence (SEM-CL) images of representative zircon grains are shown for each sample with the reported $^{206}Pb/^{238}U$ dates determined for the LA-ICP-MS spots.

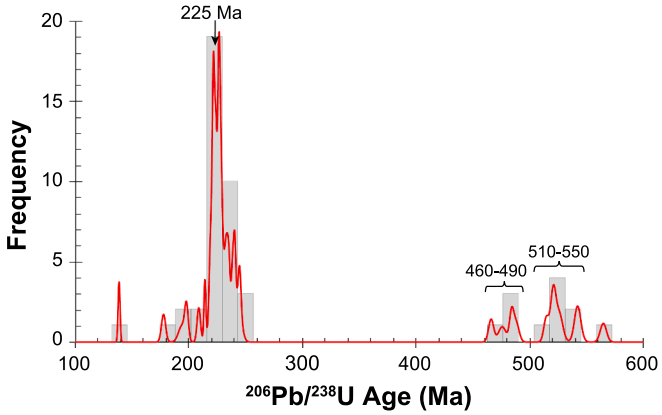

Fig. 12. Histogram and probability density distribution of ^{206}Pb/^{238}U ages of inherited magmatic zircons (n = 50) from the SRIC.

This process produced large volumes of peraluminous granitic magmas that thereafter repeatedly mixed with parental mafic melts in a shallow-crustal magma reservoir.

5.3. U—Pb zircon dates and crystallization ages of the SRIC

Our LA-ICP-MS analyses of the San Rafael megacrystic granite yielded a weighted mean ^{206}Pb/^{238}U date of 24.02 ± 0.25 Ma (Fig. 11B) on igneous-textured zircon rims and cores, which is interpreted as a crystallization age. This age is slightly younger than the previous isotope dilution – thermal ionization mass spectrometry (ID-TIMS) ^{206}Pb/^{238}U ages of 24.6 ± 0.2 Ma and 24.7 ± 0.2 Ma obtained on single monazite and zircon, respectively (Kontak and Clark, 2002). This discrepancy presumably reflects the contribution of older, inherited zircon and possibly monazite cores, accidentally analyzed by the bulk ID-TIMS measurements. Alternatively, the older ID-TIMS ages could be ascribed to a different procedure of common Pb correction. The fine-grained granite and medium-grained granite yielded weighted mean

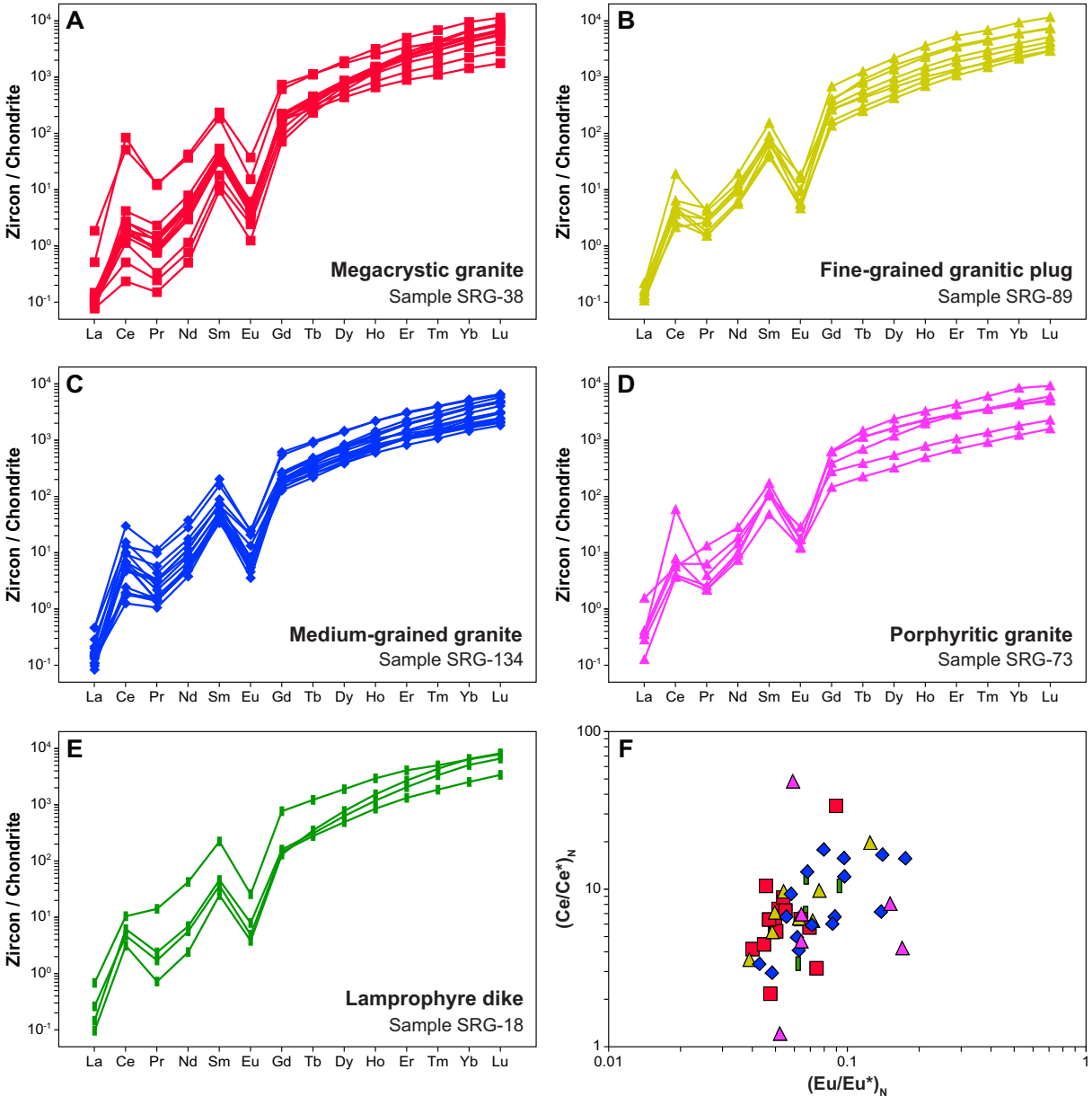

Fig. 13. Rare earth element compositions of magmatic zircons from the SRIC. Chondrite-normalizing values from McDonough and Sun (1995).

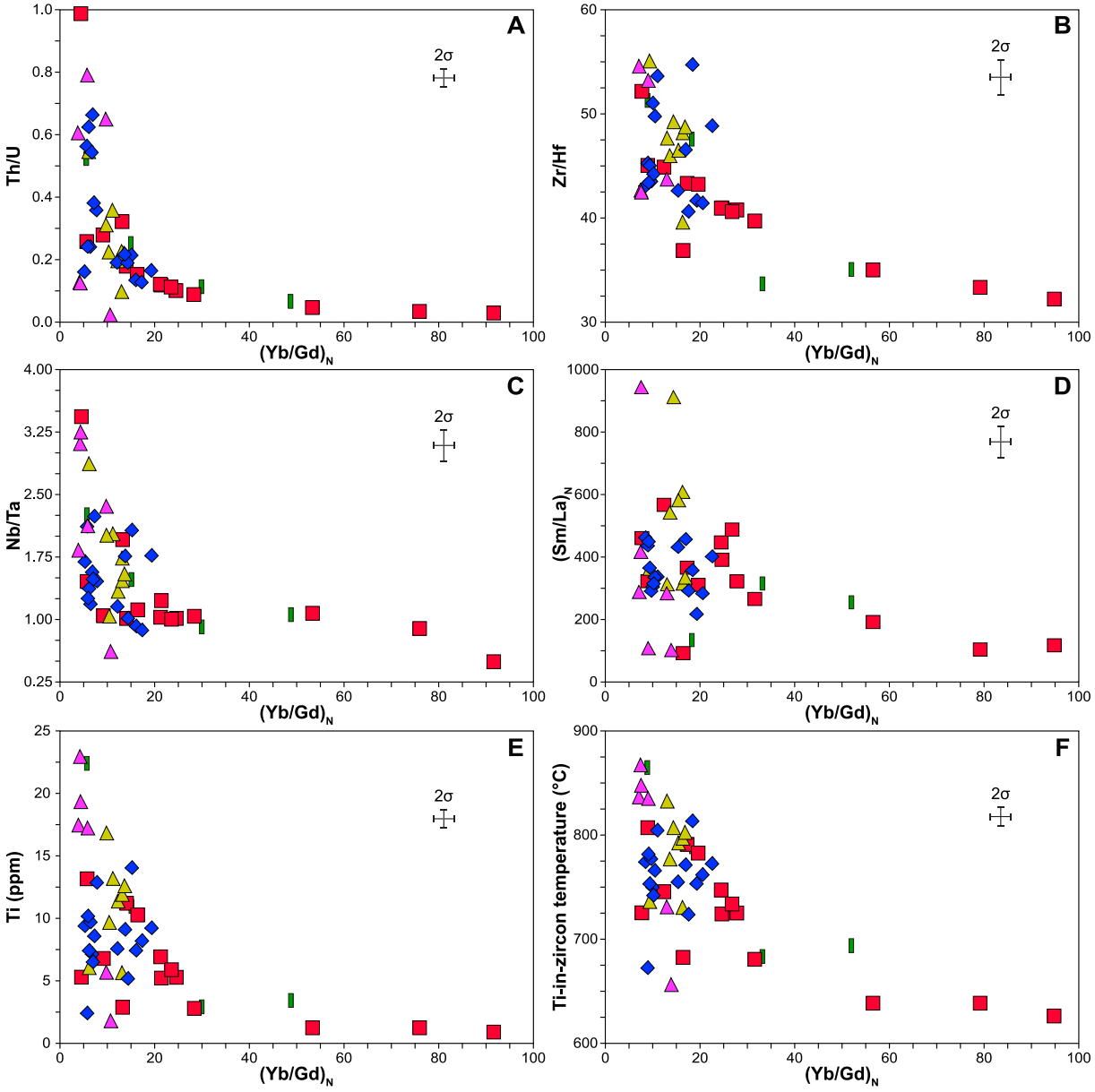

Fig. 14. Trace element variations in magmatic zircons from the SRIC. Crystallization temperatures are calculated using the Ti-in-zircon thermometer of Ferry and Watson (2007) assuming $a(SiO_2) = 1$ and $a(TiO_2) = 0.7$. Same legend as Fig. 13.

$^{206}Pb/^{238}U$ LA-ICP-MS dates of 24.17 ± 0.28 Ma and 24.26 ± 0.26 Ma, respectively (Fig. 11C–D), on oscillatory zoned igneous-textured zircon grains interpreted as crystallized from the silicate melt. These two ages are identical to each other and to that of the megacrystic granite within uncertainty, suggesting that the zircons trapped in different granitic magmas crystallized contemporaneously within the same reservoir in agreement with the field observations and textural evidence (comagmatic enclaves, dismembered dikes, mingling/mixing textures). The crystallization of the SRIC was coeval with the emplacement of mafic melts as evidenced by the presence of mingled enclaves and subvertical dikes of lamprophyres, devoid of chilled margins, which crosscut the granitic stock. The dated lamprophyre dike yielded a zircon weighted mean $^{206}Pb/^{238}U$ date of 23.79 ± 0.27 Ma (Fig. 11A), interpreted as a crystallization age. Nonetheless, this date was obtained with only four zircon LA-ICP-MS analyses and must be therefore considered with caution. It is noteworthy that this age falls in the range of 26–22 Ma, as defined by lamprophyres from the Eastern Cordillera of southeast Peru (Carlier et al., 1997, 2005; Sandeman et al., 1997; Sandeman and Clark, 2003).

The tourmaline-bearing leucogranite has not been dated due to low zircon abundance in the sampled material. This leucogranitic rock is only encountered as a single intrusive plug within the San Rafael granite and as discrete dikes in proximity to the Quenamari stock. Additionally, Kontak and Clark (2002) documented a single dike of tourmaline-bearing leucogranite crosscutting the megacrystic granite in a drill core at ca. 4300 masl. These field observations would indicate that the tourmaline-bearing leucogranite tardily intruded the SRIC during a new pulse of B-rich granitic magma. No concordant zircon age could be obtained for the porphyritic granite, which is only known at Quenamari where it postdates the megacrystic granite. Single LA-ICP-MS spots on oscillatory zircon rims from the porphyritic granite yielded $^{206}Pb/^{238}U$ dates ranging from 24.7 ± 0.5 Ma to 21.5 ± 0.2 Ma (Supplementary Table 3), but the corresponding analyses are not concordant and cannot be ascribed with certainty to a crystallization age. Nevertheless, petrographic observations and crosscutting relationships established from core logging, indicate that the porphyritic

granitic plug is strongly hydrothermally altered and was emplaced between the main Sn ore stage II and the polymetallic veining stages III and IV (ca. 22 Ma; Kontak and Clark, 2002). Future geochronological studies should focus, therefore, on better constraining the crystallization ages of these two granitic plugs to determine the overall duration of the San Rafael magmatic system. In comparison, emplacement of a cordierite-biotite granite dike at 23.81 ± 0.23 Ma and eruption of mafic lava flows at 23.39 ± 0.89 Ma are documented at Cerro Moromoroni within the Antauta Field, located only a few kilometers southeast of the SRIC (Kontak et al., 1986; Sandeman et al., 1997). This suggests that the San Rafael magmatic system may have remained protractedly active following the crystallization of the main pluton.

Many of the studied zircons in the San Rafael granitoids contain partially resorbed inherited cores surrounded by igneous-textured oscillatory zoned rims (Supplementary Fig. 4). The major peak at ca. 225 Ma, observed in the distribution of $^{206}Pb/^{238}U$ dates of inherited zircons (Fig. 12), is coeval with the opening of the Mitu Rift in southern Peru during the Triassic between 245 and 220 Ma (Spikings et al., 2016). Sediments from the Mitu Group are mainly exposed in the Altiplano and in the Eastern Cordillera of southern Peru and consist dominantly of sandstones, siliclastic mudstones, and conglomerates (Spikings et al., 2016). Opening of the Mitu Rift preceded the emplacement of Upper Triassic to Lower Jurassic (ca. 220–190 Ma) peraluminous granitoids in the Cordillera de Carabaya (Kontak et al., 1990a; Mišković et al., 2009). The oldest groups of inherited zircons from the SRIC yielded ages of 460-490 Ma and 510–550 Ma, which correspond to the Famatinian orogenic cycle that affected the Proto-Andean margin of Peru during the Cambrian to Ordovician (Chew et al., 2016 and references therein). Similar U—Pb ages were reported for detrital zircons from the Ordovician Sandia Formation in southeastern Peru (Reimann et al., 2010), the dominant lithostratigraphic unit hosting the SRIC. Most inherited zircons are interpreted, therefore, as xenocrysts derived from rift-related sediments of the Mitu Group and/or from Triassic Eastern Cordillera granitoids that were assimilated during the emplacement of the SRIC.

5.4. Fertility of the SRIC as source of Sn and Cu

The formation of granite-related Sn deposits is generally considered as resulting from extended fractional crystallization of highly evolved felsic melts followed by exsolution of Sn-rich magmatic-hydrothermal fluids (Lehmann, 2020). However, this model is hard to reconcile with the moderately fractionated character of the San Rafael granites as shown by our whole rock and zircon geochemical data. Alternatively, Sn-rich granitic melts can also be generated by biotite-controlled high-temperature (>775 °C) melting of metasedimentary protoliths, enhanced by multiple melt extractions, without the need of extreme magmatic fractionation (Wolf et al., 2018). Tin contents in the least altered San Rafael granites range between 3 and 40 ppm, with an average of 13 ppm, which corresponds to about 6.5 times the natural abundance of Sn in the UCC (Rudnick and Gao, 2014). These Sn contents fall in the same range of values as reported for “tin granites” from the Central Andean tin belt (Sn = 10–100 ppm; Lehmann et al., 1990) and quartz-hosted melt inclusions from Bolivian Sn porphyries (Sn = 5–43 ppm; Dietrich et al., 2000). Because peraluminous, ilmenite-bearing S-type granitic magmas are reduced, they can accommodate higher content of incompatible Sn^{2+} in the residual silicate melt, compared to the oxidized, magnetite-bearing I-type magmas, in which compatible Sn^{4+} is sequestered by crystallizing mineral phases and cannot be further enriched by crystal fractionation (Bhalla et al., 2005; Linnen et al., 1996). Copper contents in the least altered San Rafael granites are comprised between 5 and 62 ppm, averaging at 23 ppm, which falls within the natural abundance of Cu in the UCC (Rudnick and Gao, 2014). Almost all San Rafael granites have Zr/Hf (31–35) and Nb/Ta (4–8) ratios corresponding to the field of barren granites (Supplementary Fig. 5), as defined by Ballouard et al. (2016). Moreover, no vertical zoning and upward fractionation trend is observed in the San Rafael pluton, altogether suggesting that magmatic fractionation was insufficient for generating a Sn-rich granitic melt.

Previous fluid inclusion and stable isotope studies indicate that the mineralizing fluids forming the San Rafael Sn (—Cu) deposit are of magmatic origin (Harlaux et al., 2021; Kontak and Clark, 2002; Mlynarczyk et al., 2003; Wagner et al., 2009). Two possible genetic models can then be discussed regarding the source of fluids and metals: (i) both fluid and metals come from an unexposed magmatic body at depth, or (ii) the fluid comes from an underlying magma reservoir and has interacted with the SRIC by leaching Sn and other metals. Tin slightly partitions into moderately evolved peraluminous granitic melts (Schmidt et al., 2020) and can be incorporated in Sn-sequestering minerals such as micas, which commonly contain 10s to >100 s ppm of Sn on average (Breiter et al., 2017, 2018; Simons et al., 2017). Thus, biotite destruction during chloritization, in parts of the SRIC, may have released amounts of Sn into the hydrothermal fluid. However, this model is not compatible with the fact that chloritization of the San Rafael granite, essentially restricted within few meters along the mineralized structures, is extremely limited at the scale of the pluton (<1% volume). In addition, there is no systematic relationship between the local abundance of cassiterite and the degree of chloritization of the granitic rocks, which do not contain any disseminated cassiterite (Kontak and Clark, 2002; Mlynarczyk et al., 2003). Based on a simple mass balance calculation assuming that magmatic biotite (~10% volume of the original granite) contains initially 100 ppm of Sn on average and was completely destroyed during chloritization of the granitic pluton (~0.5% of a total granite volume estimated at ca. 100 km^3), a maximum amount of 13,500 t of Sn can be theoretically extracted from the SRIC. This amount is lower by two orders of magnitude than the >1 Mt. of Sn of past production and present resources in the San Rafael deposit. Therefore, chloritization of the granitic rocks appears more as the consequence of fluid-rock reactions with the mildly acidic mineralizing fluids rather than the sourcing mechanism of Sn.

Compared to the other granite varieties, the tourmaline-bearing leucogranite is characterized by a felsic peraluminous composition with higher SiO_2 contents and lower Fe_2O_3 and MgO contents, and higher contents of incompatible trace elements (Li, B, Ga, Rb, Cs, Nb, Ta), altogether indicating a more fractionated character. This interpretation is in accordance with the conclusions of Kontak and Clark (2002), who showed that the chemical composition of biotite in the tourmaline-bearing leucogranite deviates markedly from the one in the other granite varieties, notably by higher contents of SiO_2, Al_2O_3 and F, and lower contents of Fe_2O_3, MgO and TiO_2, which indicate a higher fractionation degree of the granitic melt. The tourmaline-bearing leucogranite also shows slightly higher Sn contents (17–45 ppm, avg. = 28 ppm) and lower Zr/Hf (21–28) and Nb/Ta (3–5) ratios (Supplementary Fig. 5) falling into the field of Sn-W-related granites from Ballouard et al. (2016). Additionally, the initially high B content of the leucogranitic melt must have lowered the solidus temperature (<680 °C, 1 kbar), reduced melt viscosity, and increased water solubility (Dingwell et al., 1996), resulting in extended magmatic differentiation and thus increased Sn content in the late-magmatic fluid. These characteristics would suggest that the tourmaline-bearing leucogranite is a more favorable source rock for the ore-forming fluids than the main biotite-cordierite megacrystic granite. However, the tourmaline-bearing leucogranite is a volumetrically minor body at the scale of the SRIC and cannot explain the high tonnage of Sn in the San Rafael deposit. The presence of a large, unexposed tourmaline-rich leucogranite body at depth remains speculative since neither underground workings nor deep drillings through the pluton evidenced such intrusion. We conclude that Sn and other metals were likely sourced from a more fractionated, deeper part of the granitic magma reservoir and that the SRIC only acted as a passive host providing the structural focusing for the mineralizing fluids, as discussed in the next section.

5.5. Role of magma mixing and genetic implications for the San Rafael Sn (—Cu) deposit

As discussed previously, the SRIC records petrographic and geochemical evidence of mingling and mixing between monzogranitic magmas and mantle-derived mafic melts. Thus, the interaction and the subsequent hybridization between reduced granitic and more oxidized mafic magmas must have strong impact on the behavior of redox-sensitive elements like Sn. That this hybridization process probably took place is suggested by compositions of biotite in nearby comparable peraluminous intrusions from the Oligocene-Miocene Crucero Supergroup. Anomalously high and variable Fe^{3+}/Fe^{2+} ratios (0.2–0.6) were determined in unaltered biotite phenocrysts from the Revancha cordierite-biotite peraluminous S-type granitic dike (ca. 24.1 Ma), located at about 25 km west of San Rafael, very similar in its major element chemistry to biotite from the SRIC, and exhibiting mineralogical, textural, and geochemical features of hybridization with mafic melts (Kontak and Clark, 2002; Sandeman and Clark, 2003). The high Fe^{3+} content of biotite, strongly contrasting with the reduced nature of the host rock (ilmenite-bearing), is interpreted by Sandeman and Clark (2003) to record late-magmatic oxidation, straddling the hematite-magnetite buffer, caused by mixing of reduced granitic magmas with more oxidized mantle-derived potassic melts. Even higher Fe^{3+}/Fe^{2+} ratios (0.4–3.5) have been reported for biotites from the highly reduced Macusani peraluminous rhyolites (ca. 10–7 Ma; Pichavant et al., 1988), located at about 25 km northwest of San Rafael, and possibly reflecting late-magmatic oxidation associated with volatile concentration before eruption (Sandeman and Clark, 2003). Late-magmatic oxidation, reflecting the increase of fO_2 conditions, has been interpreted as the consequence of water dissociation, oxygen retention in the melt, and hydrogen diffusive loss during mixing of water-saturated felsic melts with hot lamprophyric melts (Carlier and Lorand, 2008).

Injection of underplating mafic melt in a cooler, more evolved silicic melt reservoir will cause reheating and partial melting of the crystal mush, thus generating exsolution of a magmatic volatile phase that can accumulate and migrate upward through buoyant instabilities (Edmonds and Woods, 2018; Parmigiani et al., 2014). Late-magmatic oxidation, possibly caused by partial dissociation of water, will result in a decrease of Sn solubility in the melt (Bhalla et al., 2005) and reduction of the degassed volatile phase (F- and Cl-rich) by hydrogen diffusion. The combination of these two effects will induce a strong partitioning of Sn to the magmatic fluid due to elevated fluid/melt partition coefficients of Sn in reduced Cl- and F-rich aqueous solutions (Schmidt et al., 2020), thus potentially generating supersaturated Sn-rich fluids. Shallow-crustal hybridization of highly fractionated silicic melts with mantle-derived mafic melts has also been proposed as a major mechanism for the formation of Bolivian Sn porphyries based on compositions of quartz-hosted melt inclusions showing enrichment in incompatible elements such as Ta, B, Cs, Li, and Sn (Dietrich et al., 2000).

Building on the model discussed above, we propose that mingling and mixing between monzogranitic magmas and mantle-derived mafic melts played a major role for triggering the formation of the world-class San Rafael Sn (—Cu) deposit (Fig. 15). Following assembling and crystallization of the upper part of the granitic pluton, the interaction of ascending high-temperature (>1100 °C) mafic melts injected into a much cooler (>800 °C) and more reduced, fractionated granitic melt reservoir triggered late-magmatic oxidation, crystal mush reactivation, and second boiling. This resulted in the exsolution of metal-rich fluids (mainly Sn and Cu) that can ascend toward the upper part of the pluton through the crystal mush reservoir. When approaching the granitic cupola, the metal-rich fluids were channelized along subvertical dilational structures (stage I veins), where they cooled down and mixed with downwelling meteoric waters producing the Sn-(Cu) mineralized stages II and III veins and breccias during a rapid lithostatic-hydrostatic pressure transition (Harlaux et al., 2021; Kontak and Clark, 2002; Mlynarczyk et al., 2003; Wagner et al., 2009).

6. Conclusions

The SRIC is dominantly composed of a biotite-cordierite -bearing K-feldspar megacrystic granite that contains comagmatic enclaves and dismembered dikes of granites and subordinate lamprophyres. The granitic rocks have moderately fractionated peraluminous S-type compositions with strongly crustal Sr, Nd, and Pb isotopic signatures. In situ U—Pb dating and trace element analysis of zircons show that the granitic magmas crystallized contemporaneously within age uncertainty at 24.02 ± 0.25 Ma (megacrystic granite), 24.17 ± 0.28 Ma (fine-grained granite), and 24.26 ± 0.26 Ma (medium-grained granite) at Ti-in-zircon temperatures from 638° to 840 °C (avg = 759 ± 49 °C). The lamprophyres have high contents of lithophile elements (Li, Rb, Cs, Sn, W) while showing more primitive Sr—Nd isotopic compositions, indicating a metasomatized subcontinental lithospheric mantle source contaminated by crustal assimilation and/or mixing with granitic magmas. Tin contents of the main San Rafael granites are moderate (3–40 ppm; avg. = 13 ppm Sn) and fall in the same range of values as reported for “tin granites” from the Central Andean tin belt. Based on our petrological and geochemical data, we conclude that the SRIC results from partial melting of metasedimentary protoliths and hybridization with mantle-derived mafic melts. We propose that the injection of high-temperature mafic melts into a more reduced, fractionated granitic crystal mush reservoir was the major trigger for exsolving metal-rich magmatic fluids, which ascended toward the granitic cupola where they cooled down and mixed with convecting meteoric waters, thus generating the world-class San Rafael Sn (—Cu) deposit.

Supplementary data to this article can be found online at https://doi.org/10.1016/j.lithos.2021.106409.

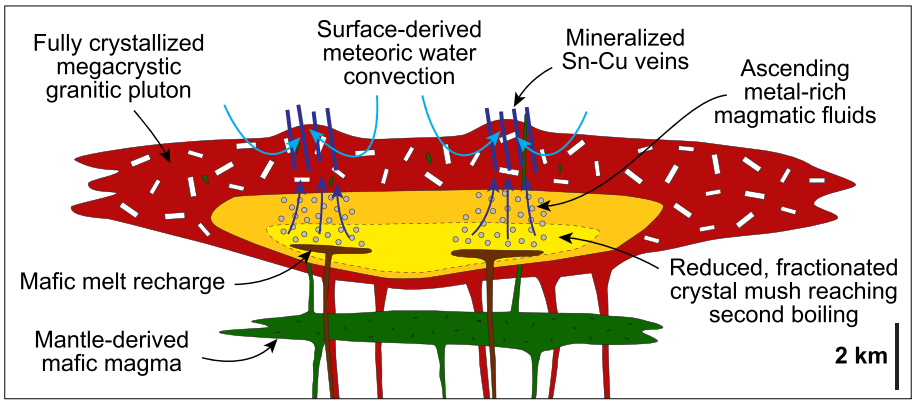

Fig. 15. Conceptual model for the formation of the San Rafael Sn (—Cu) deposit. Peraluminous S-type granitic magmas are derived from partial melting of metasedimentary rocks in a relatively thin continental crust, possibly induced by an anomalous asthenospheric heat flow and underplating of mantle-derived mafic magmas. Following assembling and crystallization of the upper part of the granitic pluton, magma recharge by high-temperature mafic melts triggered second boiling into the fractionated crystal mush reservoir and exsolution of metal-rich magmatic fluids. The latter ascended toward the granitic cupola where they cooled down and mixed with convecting meteoric waters, thus producing the Sn—Cu mineralized veins.

Declaration of Competing Interest

The authors declare that they have no known competing financial interests or personal relationships that could have appeared to influence the work reported in this paper.

Acknowledgements

This research was supported by the Swiss National Science Foundation (grant SNSF S19053_169901) and the company Minsur S.A. Logistical assistance in the field was provided by the geologist teams from Minsur S.A., who are gratefully acknowledged here. We also thank Jean-Marie Boccard for preparation of high-quality thin sections and Fabio Capponi for the XRF analyses. We are grateful to Dr. Karel Breiter and another anonymous reviewer as well as to the Co-Editor-in-Chief Dr. Greg Shellnutt for their constructive comments which greatly helped us in improving the original manuscript.

References

Abdelfadil, K.M., Romer, R.L., Seifert, T., Lobst, R., 2013. Calc-alkaline lamprophyres from Lusatia (Germany) - evidence for a repeatedly enriched mantle source. Chem. Geol. 353, 230–245.

Audétat, A., Günther, D., Heinrich, C.A., 2000. Magmatic-hydrothermal evolution in a fractionating granite: a microchemical study of the Sn-W-F-mineralized Mole Granite (Australia). Geochim. Cosmochim. Acta 64, 3373–3393.

Ballouard, C., Poujol, M., Boulvais, P., Branquet, Y., Tartèse, R., Vigneresse, J.L., 2016. Nb-Ta fractionation in peraluminous granites: a marker of the magmatic-hydrothermal transition. Geology 44, 231–234.

Barbarin, B., 1999. A review of the relationships between granitoid types, their origins and their geodynamic environments. Lithos 46, 605–626.

Bhalla, P., Holtz, F., Linnen, R.L., Behrens, H., 2005. Solubility of cassiterite in evolved granitic melts: effect of T, fO_2, and additional volatiles. Lithos 80, 387–400.

Bonin, B., Janoušek, V., Moyen, J.F., 2020. Chemical variation, modal composition and classification of granitoids. Geol. Soc. Lond., Spec. Publ. 491, 9–51.

Breiter, K., Lamarão, C.N., Borges, R.M.K., Dall'Agnol, R., 2014. Chemical characteristics of zircon from A-type granites and comparison to zircon of S-type granites. Lithos 192, 208–225.

Breiter, K., Ďurišová, J., Hrstka, T., Korbelová, Z., Vaňková, M.H., Galiová, M.V., Kanický, V., Rambousek, P., Knésl, I., Dobeš, P., Dosbaba, M., 2017. Assessment of magmatic vs. metasomatic processes in rare-metal granites: a case study of the Cínovec/Zinnwald Sn–W–Li deposit, Central Europe. Lithos 292, 198–217.

Breiter, K., Ďurišová, J., Hrstka, T., Korbelová, Z., Galiová, M.V., Müller, A., Simons, B., Shail, R.K., Williamson, B.J., Davies, J.A., 2018. The transition from granite to banded aplite-pegmatite sheet complexes: an example from Megiliggar Rocks, Tregonning topaz granite, Cornwall. Lithos 302, 370–388.

Buret, Y., von Quadt, A., Heinrich, C., Selby, D., Wälle, M., Peytcheva, I., 2016. From a long-lived upper-crustal magma chamber to rapid porphyry copper emplacement: Reading the geochemistry of zircon crystals at Bajo de la Alumbrera (NW Argentina). Earth Planet. Sci. Lett. 450, 120–131.

Carlier, G., Lorand, J.P., 2008. Zr-rich accessory minerals (titanite, perrierite, zirconolite, baddeleyite) record strong oxidation associated with magma mixing in the south Peruvian potassic province. Lithos 104, 54–70.

Carlier, G., Lorand, J.P., Audebaud, E., Kienast, J.R., 1997. Petrology of an unusual orthopyroxene-bearing minette suite from southeastern Peru, Eastern Andean Cordillera: Al-rich lamproites contaminated by peraluminous granites. J. Volcanol. Geotherm. Res. 75, 59–87.

Carlier, G., Lorand, J.P., Liégeois, J.P., Fornari, M., Soler, P., Carlotto, V., Cardenas, J., 2005. Potassic-ultrapotassic mafic rocks delineate two lithospheric mantle blocks beneath the southern Peruvian Altiplano. Geology 33, 601–604.

Chappell, B.W., White, A.J.R., 1992. I- and S-type granites in the Lachlan Fold Belt. Trans. R. Soc. Edinb. Earth Sci. 83, 1–26.

Chelle-Michou, C., Chiaradia, M., Ovtcharova, M., Ulianov, A., Wotzlaw, J.F., 2014. Zircon petrochronology reveals the temporal link between porphyry systems and the magmatic evolution of their hidden plutonic roots (the Eocene Coroccohuayco deposit, Peru). Lithos 198, 129–140.

Chew, D.M., Pedemonte, G., Corbett, E., 2016. Proto-Andean evolution of the Eastern Cordillera of Peru. Gondwana Res. 35, 59–78.

Chiaradia, M., Müntener, O., Beate, B., 2020. Effects of aseismic ridge subduction on the geochemistry of frontal arc magmas. Earth Planet. Sci. Lett. 531, 115984.

Claiborne, L.L., Miller, C.F., Wooden, J.L., 2010. Trace element composition of igneous zircon: a thermal and compositional record of the accumulation and evolution of a large silicic batholith, Spirit Mountain, Nevada. Contrib. Mineral. Petrol. 160, 511–531.

Clark, A.H., Kontak, D.J., 2004. Fe-Ti-P oxide melts generated through magma mixing in the Antauta subvolcanic center, Peru: implications for the origin of nelsonite and iron oxide-dominated hydrothermal deposits. Econ. Geol. 99, 377–395.

Clark, A.H., Palma, V.V., Archibald, D.A., Farrar, E., Arenas, F.M.J., Robertson, R.C., 1983. Occurrence and age of tin mineralization in the Cordillera Oriental, southern Peru. Econ. Geol. 78, 514–520.

Clark, A.H., Farrar, E., Kontak, D.J., Langridge, R.J., Arenas, F.M.J., France, L.J., McBride, S.L., Woodman, P.L., Wasteneys, H.A., Sandeman, H.A., Archibald, D.A., 1990. Geologic and geochronologic constraints on the metallogenic evolution of the Andes of southeastern Peru. Econ. Geol. 85, 1520–1583.

Deering, C.D., Bachmann, O., 2010. Trace element indicators of crystal accumulation in silicic igneous rocks. Earth Planet. Sci. Lett. 297, 324–331.

Dietrich, A., Lehmann, B., Wallianos, A., 2000. Bulk rock and melt inclusion geochemistry of Bolivian tin porphyry systems. Econ. Geol. 95, 313–326.

Dingwell, D.B., Pichavant, M., Holtz, F., 1996. Experimental studies of boron in granitic melts. Rev. Mineral. 33, 331–385.

Edmonds, M., Woods, A.W., 2018. Exsolved volatiles in magma reservoirs. J. Volcanol. Geotherm. Res. 368, 13–30.

Farina, F., Stevens, G., Dini, A., Rocchi, S., 2012. Peritectic phase entrainment and magma mixing in the late Miocene Elba Island laccolith–pluton–dyke complex (Italy). Lithos 153, 243–260.

Ferry, J.M., Watson, E.B., 2007. New thermodynamic models and revised calibrations for the Ti-in-zircon and Zr-in-rutile thermometers. Contrib. Mineral. Petrol. 154, 429–437.

Gao, P., Zheng, Y.F., Zhao, Z.F., 2016. Distinction between S-type and peraluminous I-type granites: Zircon versus whole rock geochemistry. Lithos 258, 77–91.

Gemmrich, L., Torró, L., Melgarejo, J.C., Laurent, O., Vallance, J., Chelle-Michou, C., Sempere, T.P., 2021. Trace element composition and U-Pb ages of cassiterite from the Bolivian tin belt. Mineral. Deposita. https://doi.org/10.1007/s00126-020-01030-3.

Guillong, M., Meier, D.L., Allan, M.M., Heinrich, C.A., Yardley, B.W.D., 2008. SILLS: A MATLAB-based program for the reduction of laser ablation ICP-MS data of homogeneous materials and inclusions. In: Sylvester, P. (Ed.), Laser Ablation ICP-MS in the Earth Sciences: Current Practices and Outstanding Issues: Mineralogical Association of Canada Short Course Series, vol. 40, pp. 328–333.

Guillong, M., Wotzlaw, J.-F., Looser, N., Laurent, O., 2020. Evaluating the reliability of U–Pb laser ablation inductively coupled plasma mass spectrometry (LA-ICP-MS) carbonate geochronology: Matrix issues and a potential calcite validation reference material. Geochronology 2, 155–167.

Harlaux, M., Kouzmanov, K., Gialli, S., Laurent, O., Rielli, A., Dini, A., Chauvet, A., Menzies, A., Kalinaj, M., Fontboté, L., 2020. Tourmaline as a tracer of late-magmatic to hydrothermal fluid evolution: the world-class San Rafael tin (−copper) deposit, Peru. Econ. Geol. 115, 1665–1697.

Harlaux, M., Kouzmanov, K., Gialli, S., Marger, K., Bouvier, A.S., Baumgartner, L.P., Rielli, A., Dini, A., Chauvet, A., Kalinaj, M., Fontboté, L., 2021. Fluid mixing as primary trigger for cassiterite deposition: evidence from in situ $\delta^{18}O$-$\delta^{11}B$ analysis of tourmaline from the world-class San Rafael tin (−copper) deposit, Peru. Earth Planet. Sci. Lett. 563, 116889.

Hayden, L.A., Watson, E.B., 2007. Rutile saturation in hydrous siliceous melts and its bearing on Ti-thermometry of quartz and zircon. Earth Planet. Sci. Lett. 258, 561–568.

Horstwood, M.S., Košler, J., Gehrels, G., Jackson, S.E., McLean, N.M., Paton, C., Pearson, N.J., Sircombe, K., Sylvester, P., Vermeesch, P., Bowring, J.F., 2016. Community-derived standards for LA-ICP-MS U-(Th-) Pb geochronology–uncertainty propagation, age interpretation and data reporting. Geostand. Geoanal. Res. 40, 311–332.

Hoskin, P.W., Schaltegger, U., 2003. The composition of zircon and igneous and metamorphic petrogenesis. Rev. Mineral. Geochem. 53, 27–62.

Kamenov, G., Macfarlane, A.W., Riciputi, L., 2002. Sources of lead in the San Cristobal, Pulacayo, and Potosi mining districts, Bolivia, and a reevaluation of regional ore lead isotope provinces. Econ. Geol. 97, 573–592.

Kontak, D.J., Clark, A.H., 1997. The Minastira peraluminous granite, Puno, southeastern Peru: a quenched, hypabyssal intrusion recording magma commingling and mixing. Mineral. Mag. 61, 743–764.

Kontak, D.J., Clark, A.H., 2002. Genesis of the giant, bonanza San Rafael lode tin deposit, Peru: origin and significance of pervasive alteration. Econ. Geol. 97, 1741–1777.

Kontak, D.J., Clark, A.H., Farrar, E., Pearce, T.H., Strong, D.F., Baadsgaard, H., 1986. Petrogenesis of a Neogene shoshonite suite, Cerro Moromoroni, Puno, southeastern Peru. Can. Mineral. 24, 117–135.

Kontak, D.J., Clark, A.H., Farrar, E., Archibald, D.A., Baadsgaard, H., 1987. Geochronological data for Tertiary granites of the Southeast Peru segment of the central Andean tin belt. Econ. Geol. 82, 1611–1618.

Kontak, D.J., Clark, A.H., Farrar, E., Archibald, D.A., Baadsgaard, H., 1990a. Late Paleozoic-early Mesozoic magmatism in the Cordillera de Carabaya, Puno, southeastern Peru: geochronology and petrochemistry. J. S. Am. Earth Sci. 3, 213–230.

Kontak, D.J., Cumming, G.L., Krstic, D., Clark, A.H., Farrar, E., 1990b. Isotopic composition of lead in ore deposits of the Cordillera Oriental, southeastern Peru. Econ. Geol. 85, 1584–1603.

Lehmann, B., 2020. Formation of tin ore deposits: a reassessment. Lithos 105756.

Lehmann, B., Ishihara, S., Michel, H., Miller, J., Rapela, C.W., Sanchez, A., Tistl, M., Winkelmann, L., 1990. The Bolivian tin province and regional tin distribution in the Central Andes; a reassessment. Econ. Geol. 85, 1044–1058.

Linnen, R.L., Pichavant, M., Holtz, F., 1996. The combined effects of fO_2 and melt composition on SnO_2 solubility and tin diffusivity in haplogranitic melts. Geochim. Cosmochim. Acta 60, 4965–4976.

Loucks, R.R., Fiorentini, M.L., Henríquez, G.J., 2020. New magmatic oxybarometer using trace elements in zircon. J. Petrol. 61 egaa034.

Macfarlane, A.W., Marcet, P., LeHuray, A.P., Petersen, U., 1990. Lead isotope provinces of the Central Andes inferred from ores and crustal rocks. Econ. Geol. 85, 1857–1880.

Mamani, M., Wörner, G., Sempere, T., 2010. Geochemical variations in igneous rocks of the Central Andean orocline (13°S to 18°S): Tracing crustal thickening and magma generation through time and space. GSA Bull. 122, 162–182.
Mayne, M.J., Stevens, G., Moyen, J.F., 2020. A phase equilibrium investigation of selected source controls on the composition of melt batches generated by sequential melting of an average metapelite. Geol. Soc. Lond., Spec. Publ. 491, 223–241.
McDonough, W.F., Sun, S.S., 1995. The composition of the Earth. Chem. Geol. 120, 223–253.
Mišković, A., Spikings, R.A., Chew, D.M., Košler, J., Ulianov, A., Schaltegger, U., 2009. Tectonomagmatic evolution of Western Amazonia: Geochemical characterization and zircon U-Pb geochronologic constraints from the Peruvian Eastern Cordilleran granitoids. Geol. Soc. Am. Bull. 121, 1298–1324.
Mlynarczyk, M.S., 2005. Constraints on the Genesis of Lode-Style Tin Mineralization: Evidence from the San Rafael Tin-Copper Deposit. Peru: Unpublished Ph.D. thesis, McGill University, Montréal, Canada, 360 p.
Mlynarczyk, M.S., Sherlock, R.L., Williams-Jones, A.E., 2003. San Rafael, Peru: geology and structure of the worlds richest tin lode. Mineral. Deposita 38, 555–567.
Parmigiani, A., Huber, C., Bachmann, O., 2014. Mush microphysics and the reactivation of crystal-rich magma reservoirs. J. Geophys. Res. Solid Earth 119, 6308–6322.
Petrus, J.A., Kamber, B.S., 2012. VizualAge: a novel approach to laser ablation ICP-MS U-Pb geochronology data reduction. Geostand. Geoanal. Res. 36, 247–270.
Pettke, T., Audétat, A., Schaltegger, U., Heinrich, C.A., 2005. Magmatic-to-hydrothermal crystallization in the W–Sn mineralized Mole Granite (NSW, Australia): part II: evolving zircon and thorite trace element chemistry. Chem. Geol. 220, 191–213.
Pichavant, M., Kontak, D.J., Valencia-Herrara, J., Clark, A.H., 1988. The Miocene-Pliocene Macusani volcanics, SE Peru. I. Mineralogy and magmatic evolution of a two-mica aluminosilicate-bearing ignimbrite suite. Contrib. Mineral. Petrol. 100, 300–324.
Quang, C.X., Clark, A.H., Lee, J.K.W., Hawkes, N., 2005. Response of supergene processes to episodic Cenozoic uplift, pediment erosion, and ignimbrite eruption in the porphyry copper province of southern Peru. Econ. Geol. 100, 87–114.
Ramos, V.A., 2018. Tectonic evolution of the Central Andes: From terrane accretion to crustal delamination. In: Zamora, G., McClay, K.M., and Ramos, V.A. (Eds.), Petroleum Basins and Hydrocarbon Potential of the Andes of Peru and Bolivia, 117. American Association of Petroleum Geologists Memoir, pp. 1–34.
Reimann, C.R., Bahlburg, H., Kooijman, E., Berndt, J., Gerdes, A., Carlotto, V., Lopez, S., 2010. Geodynamic evolution of the early Paleozoic Western Gondwana margin 14–17 S reflected by the detritus of the Devonian and Ordovician basins of southern Peru and northern Bolivia. Gondwana Res. 18, 370–384.
Romer, R.L., Kroner, U., 2016. Phanerozoic tin and tungsten mineralization—tectonic controls on the distribution of enriched protoliths and heat sources for crustal melting. Gondwana Res. 31, 60–95.
Rudnick, R.L., Gao, S., 2014. Composition of the continental crust. In: Holland, H.D., Turekian, K.K. (Eds.), Treatise on Geochemistry, , Second edition4. Elsevier, Amsterdam, pp. 1–51.
Ryan, J., Beck, S., Zandt, G., Wagner, L., Minaya, E., Tavera, H., 2016. Central Andean crustal structure from receiver function analysis. Tectonophysics 682, 120–133.
Sandeman, H.A., Clark, A.H., 2003. Glass-rich, cordierite–biotite rhyodacite, Valle Ninahuisa, Puno, SE Peru: Petrological evidence for hybridization of 'Lachlan S-type' and potassic mafic magmas. J. Petrol. 44, 355–385.
Sandeman, H.A., Clark, A.H., 2004. Commingling and mixing of S-type peraluminous, ultrapotassic and basaltic magmas in the Cayconi volcanic field, Cordillera de Carabaya, SE Peru. Lithos 73, 187–213.
Sandeman, H.A., Clark, A.H., Farrar, E., 1995. An integrated tectono-magmatic model for the evolution of the southern Peruvian Andes (13–20°S) since 55 Ma. Int. Geol. Rev. 37, 1039–1073.
Sandeman, H.A., Clark, A.H., Farrar, E., Pauca, G.A., 1997. Lithostratigraphy, petrology and ^{40}Ar-^{39}Ar geochronology of the Crucero Supergroup, Puno department, SE Peru. J. S. Am. Earth Sci. 10, 223–245.
Schmidt, C., Romer, R.L., Wohlgemuth-Ueberwasser, C.C., Appelt, O., 2020. Partitioning of Sn and W between granitic melt and aqueous fluid. Ore Geol. Rev. 117, 103263.
Simons, B., Andersen, J.C., Shail, R.K., Jenner, F.E., 2017. Fractionation of Li, Be, Ga, Nb, Ta, In, Sn, Sb, W and Bi in the peraluminous Early Permian Variscan granites of the Cornubian Batholith: precursor processes to magmatic-hydrothermal mineralisation. Lithos 278, 491–512.
Spikings, R., Reitsma, M.J., Boekhout, F., Mišković, A., Ulianov, A., Chiaradia, M., Gerdes, A., Schaltegger, U., 2016. Characterisation of Triassic rifting in Peru and implications for the early disassembly of western Pangaea. Gondwana Res. 35, 124–143.
Spiske, M., Reinmann, C., Bahlburg, H., Carlotto, V., 2006. Sedimentology and facies analysis of the Ordovician San José and Sandia Formations in the Sandia region, Eastern Cordillera of southern Peru. Bol. Soc. Geol. Perú 101, 121–138.
Stevens, G., Villaros, A., Moyen, J.F., 2007. Selective peritectic garnet entrainment as the origin of geochemical diversity in S-type granites. Geology 35, 9–12.
Sundell, K.E., Saylor, J.E., Lapen, T.J., Horton, B.K., 2019. Implications of variable late Cenozoic surface uplift across the Peruvian Central Andes. Sci. Rep. 9, 1–12.
Szymanowski, D., Fehr, M.A., Guillong, M., Coble, M.A., Wotzlaw, J.F., Nasdala, L., Ellis, B.S., Bachmann, O., Schönbächler, M., 2018. Isotope-dilution anchoring of zircon reference materials for accurate Ti-in-zircon thermometry. Chem. Geol. 481, 146–154.
Trail, D., Watson, E.B., Tailby, N.D., 2012. Ce and Eu anomalies in zircon as proxies for the oxidation state of magmas. Geochim. Cosmochim. Acta 97, 70–87.
Wagner, T., Mlynarczyk, M.S., Williams-Jones, A.E., Boyce, A.J., 2009. Stable isotope constraints on ore formation at the San Rafael tin-copper deposit, Southeast Peru. Econ. Geol. 104, 223–248.
Wolf, M., Romer, R.L., Franz, L., López-Moro, F.J., 2018. Tin in granitic melts: the role of melting temperature and protolith composition. Lithos 310, 20–30.
Wotzlaw, J.F., Schaltegger, U., Frick, D.A., Dungan, M.A., Gerdes, A., Günther, D., 2013. Tracking the evolution of large-volume silicic magma reservoirs from assembly to supereruption. Geology 41, 867–870.
Zartman, R.E., Doe, B.R., 1981. Plumbotectonics—the model. Tectonophysics 75, 135–162.